Structuring coatings for leading edge protection inspired by erosion-resistant organisms

Merijn Egbert Otterman

Delft University of Technology

TU Delft

Structuring coatings for leading edge protection inspired by erosion-resistant organisms

by

Merijn Egbert Otterman

to obtain the degree of:

Master of Science
in Aerospace engineering
at Delft University of Technology

Master of Science
in Engineering (Wind Energy)
at the Technical University of Denmark

to be defended publicly on Thursday May 30 , 2024 at 9:30 AM.

Student number:	5611091	
Project duration:	November, 2022 – May, 2024	
Thesis committee:	Assoc. Prof. J. J. E. Teuwen	TU Delft - supervisor
	Assoc. Prof. L. P. Mikkelsen	DTU - supervisor
	Assoc. Prof. C. D. Rans	TU Delft
	Prof. E. Lund	Aalborg University
Co-supervisors:	N. S. G. Sotelo	TU Delft
	T. W. Hamers	DTU

An electronic version of this thesis is available at http://repository.tudelft.nl/.

Summary

With the wind energy sector and its turbines steadily growing in size, erosion due to the impact of rain and other types of erosion are becoming an increasingly costly problem. The damage caused by this so-called Leading-Edge Erosion often needs costly repairs, as an eroded edge has a significant impact on a turbine's annual energy production.

Currently, all leading edge protection systems consist of smooth, isotropic materials. In contrast, erosion-resistant organisms often have non-smooth structures that protect them from erosion. This thesis aims to analyse if coatings with structures inspired by erosion resistant organisms can improve the performance of the leading edge. Examples of these organisms are the desert scorpion and tamarisk tree, both very resistant to erosion by sand storms. This is studied by doing both experimental tests using a pulsating jet erosion tester, as well as numerical studies using a coupled FEM-SPH model.

The geometries selected consist of plates with long slanted grooves in them. To study the impact of different parameters, the angle, height, spacing, and impact location of these slanted surfaces were varied. Samples of these different geometries were constructed and coated using a polyurethane coating used for leading edge protection. These samples were then tested for their erosion resistance, by obtaining the incubation times using the erosion tester. In addition, the damage was inspected, and the layer thickness of the coating was measured.

To better understand the impact mechanics of the droplet impacting the structured surfaces, a coupled FEM-SPH model was used. This model can accurately model the forces and stresses involved in a high-speed droplet impact. An SPH model uses coupled small particles instead of a fixed mesh, making it suitable for high-deformation impacts such as water droplet impacts.

By combining the data from the experiments and simulations it was found that the erosion resistance could indeed be improved using the slanted surfaces. It was found that the middle of the slanted surfaces performed as expected by theory; however, for the top and valley impact locations, this was more complex. Large stresses occur in the valley impacts, which negatively affect the incubation times when the layer thickness is equal. On the other hand, tops are expected to have higher incubation times compared to the middle locations. However, this was not observed in this study as the layer thickness at the top was significantly thinner.

The results of the varying angled surfaces showed that changing the angle had a dramatic effect on the incubation time. However, due to the sizes of the slanted surfaces chosen, this was not experimentally found for all samples. It was found that once the size of the features came close to the size of the droplet, the effects of the top and valley of the slanted surfaces started negatively affecting the incubation time.

Lastly, it was found that when the distance between the slanted surfaces was increased, the effects of the top and valley disappeared. This has the potential to further increase the erosion resistance of the slanted surfaces and is recommended for future study. In conclusion, it was found that leading edge erosion resistance can indeed be improved by using structured surfaces inspired by erosion-resistant organisms.

Contents

List of Figures

List of Tables

Nomenclature

Abbreviations

Abbreviation	Definition
AEP	Annual energy production
EOS	Equation of state
FDM	Fused deposition modeling
FEM	Finite element method
GFRP	Glass fiber reinforced polymer
LEE	Leading edge erosion
LEP	Leading edge protection
PDF	Probability density function
PJET	Pulsating jet erosion tester
PU	Polyurethane
SPH	Smoothed particle hydrodynamics

Symbols

Symbol	Definition	Unit
a	Feature angle	[°]
a_1, a_2	Constants in springer model	[-]
b	Fatigue knee	[-]
C	B-spline function constant	[-]
C	Speed of sound in a material	[m/s]
d	Diameter	[m]
h	Feature height	[mm]
h	Smoothing length	[m]
L_{droplet}	Droplet length	[m]
m	Particle mass	[kg]
n	Number of impacts	[-]
P	Impact stress	[Pa]
r	Droplet radius	[m]
R	Surface radius	[m]
s	Feature spacing	[-]
S	Fatigue strength	[Pa]
T	Time	[s]
V	Velocity	[m/s]
α	Disc opening angle	[rad]
ν	Poisson's ratio	[-]
ω	Disc rotational speed	[rad/s]
ψ	Impedance parameter	[-]
ρ	Density	[kg/m^3]
σ_U	Ultimate strength	[Pa]
θ	Impact angle	[°]

1

Introduction

Wind energy production has grown significantly in recent years, thereby becoming an increasingly important source of renewable energy globally. The overall installed wind power capacity has grown tremendously and many countries have set ambitious goals to transition to renewable energy sources. To reduce the cost of wind energy and increase energy production, manufacturers continuously look for ways to improve. As a result, wind turbines have grown in size in the last few decades, as illustrated in Figure 1.1. With this, the tip speeds have also increased. Tip speeds higher than 90 m/s are not uncommon and they are only expected to increase as wind turbines grow.

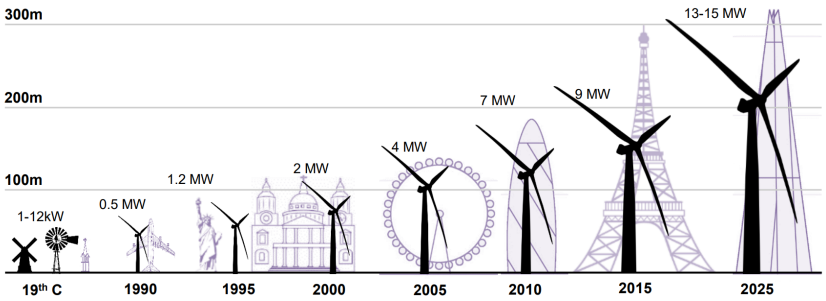

Figure 1.1: Growth in wind turbine size in the last decades. From: [25]

A downside is that these high tip speeds result in a higher impact velocity of erodents such as hail, sand, and rain. The leading edge of the wind turbine blade is the part of the wind turbine that first meets the incoming air. The leading edge is also the part that experiences the most damage, Figure 1.2 shows an example of this damage. This phenomenon is often called leading edge erosion (LEE). The rough surface on the blade increases the drag coefficient and decreases the lift coefficient of the blade, which reduces wind turbine efficiency and annual energy production (AEP). Sareen et al. [26] found decreases in AEP of 3-5% due to light to moderate damage and decreases up to 25% due to severe damage. When left untreated, LEE can amount to significant losses in the total energy production over the turbine's lifetime. While manufacturers expect blades to last at least 20 years, damage due to leading edge erosion can, according to Verma et al. [27], already appear after only two years of service. This leads to regular required repair and maintenance of the turbine blades. These repairs are expensive, especially since modern turbines are frequently located in remote and difficult-to-access locations, such as offshore. More effective solutions against leading edge erosion must be developed to make wind turbines a more competitive energy source.

Figure 1.2: An example of leading edge erosion. Source: [24]

Wind turbines, however, are not the only structures impacted by erosion. Several organisms have evolved to be very erosion-resistant against sandstorms, as was described by Han et al. [14]. The desert scorpion and the Tamarisk tree stand out especially. They are highly resistant to erosion from sandstorms, which consist of, similar to rain storms, relatively small particles impacting at high velocities. Therefore, the idea was proposed to combine these two types of erosion to contribute to the knowledge on leading edge erosion by finding out if bio-inspired surface features could enhance the erosion resistance of wind turbine blades.

1.1. Research question

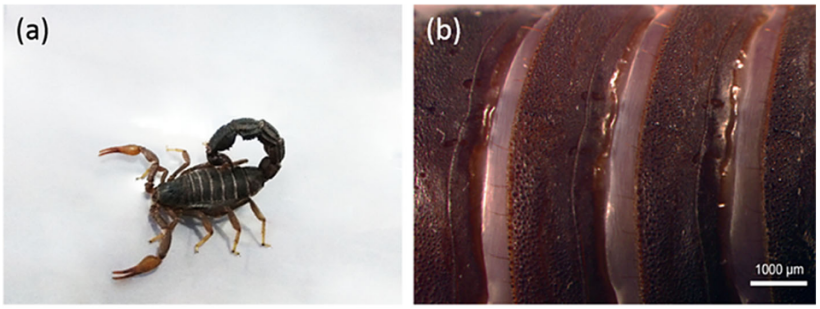

Figure 1.3: Desert scorpion with erosion-resistant grooves on its carapace. From [39]

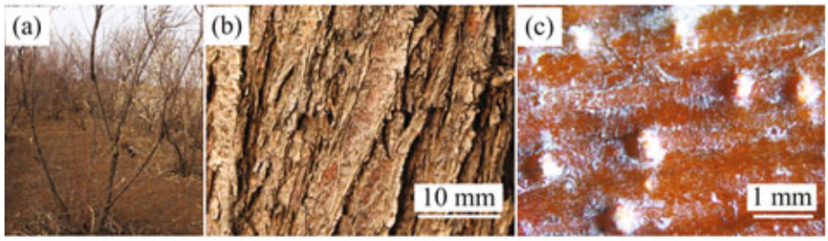

Figure 1.4: Tamarisk with erosion-resistant grooves in its bark. From [16]

When studying the anti-erosion mechanisms of the desert scorpion and tamarisk, it was found that they rely on a local change in impact angle of the particle and the generation of vortices. They achieve these characteristics by the presence of grooves in their respective carapace and bark, as is shown in Figure 1.3 and 1.4. The parallels to LEE can be seen, as it is also heavily dependent on the impact angle, and there is wind, which can generate vortices. It is interesting to study if the erosion resistance against liquid droplet erosion can be improved using features inspired by these organisms. The main

research questions thus become:

How does integrating slanted surfaces to the surface morphology, inspired by erosion-resistant organisms, impact the resistance to leading edge erosion in wind turbine blades?

An infinite amount of surface features can change the impact angle. Similarly to other biomimetic studies, the surface morphology is kept as simple as possible to improve the chances of determining the effect of different factors. This means 2-dimensional features with a constant angle, i.e., a triangle. Since the erosion resistance depends on the impact angle, this parameter will be studied. In addition, it is expected that the effect of the features depends on the height of the features. Once their size is close to that of a droplet diameter, it is expected that the top and valley will play a role, and the erosion will no longer behave similarly to an angled plate. Lastly, it is seen in nature that the features are often not directly adjacent but have a spacing between them. For this reason, it is also studied here. This leads to the following sub-questions:

- How is the erosion resistance affected by the impact location?
- How does the angle of the slanted surfaces affect the erosion resistance?
- How does the height of the slanted surfaces affect the erosion resistance?
- How does the spacing between the slanted surfaces affect the erosion resistance?

It is hypothesized that the change in angle will significantly affect the erosion resistance, as this directly correlates with the water hammer pressure. This will be especially true at the midpoint of the features. At the top and valley of the feature, the dependence on the angle is unknown. For the height, it is hypothesized that there is no large impact on the erosion resistance. However, if the feature size approaches that of the droplet size, this might result in more complex interactions that will change the erosion resistance. The spacing between the features is expected to affect the erosion resistance only if erosion due to interaction at the peak and valley is observed.

1.2. Thesis outline

To study the above-mentioned research questions, the thesis will start by investigating the underlying theory and methods to study leading edge erosion and erosion resistance in nature in Chapter 2. After this, the methodology for studying the research questions experimentally and numerically will be discussed in Chapter 3. In Chapter 4 the experimental and numerical analysis findings will be discussed. These findings will be concluded in Chapter 5.

2

State of the art

This section will cover the current state of the art of leading edge erosion of wind turbine blades as well as erosion of organisms. This is done by first explaining the buildup of a wind turbine blade in Section 2.1. Next, in Section 2.2, rain will be discussed as this is the most prominent erodent for wind turbines. Following this, in section 2.3, the mechanics of an impacting rain droplet will be discussed. After this, the test methods and current solutions to leading edge erosion are discussed in Section 2.4 and 2.5. Having now discussed the wind turbine related erosion, multiple occurrences of erosion in nature, including a section on biomimic design, are discussed in section 2.6.

2.1. Wind turbine blade buildup

To understand how erosion affects a wind turbine blade, first the buildup of the blade is discussed. An overview of a typical blade build-up is shown in figure 2.1. The blade typically has an aerofoil-shaped cross-section, being very thick at the root and becoming shorter and thinner towards the tip. To reduce the impact of gravitational forces, the blade is made from a lightweight composite material, usually a glass fibre-reinforced polymer (GFRP). The blade cross-section consists of an aerofoil-shaped skin and multiple load-bearing shear webs. The front of the blade, which faces the incoming wind is called the leading edge, and the rearward part is the trailing edge. Since the leading edge is the part of the blade that faces the incoming wind, it also experiences the most erosion from airborne erodents. Especially near the tip of the blade, where the speeds due to the rotor rotation are the highest. This is why the erosion phenomenon is called leading edge erosion.

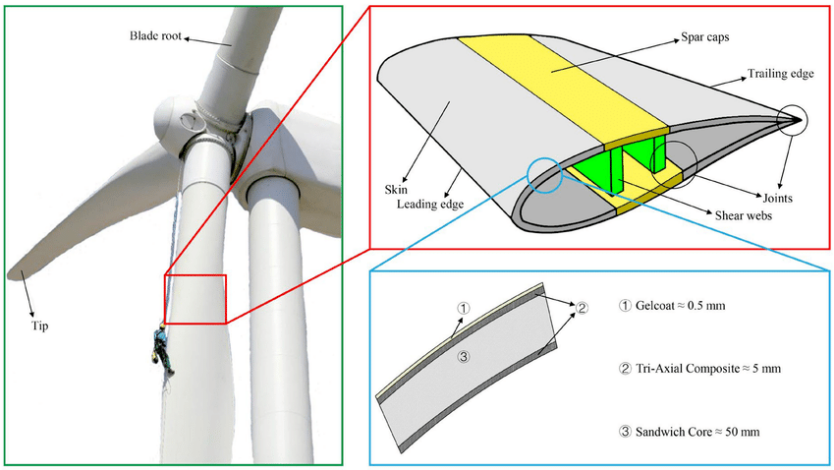

Figure 2.1: Overview of typical wind turbine blade construction, from [7]

.

2.2. Rain droplet parameters

Since rain is the most often occurring erodent for leading edge erosion of wind turbine blades,this thesis will focus on the impact and damage of rain in particular. To understand rain erosion, it is important to first consider the rain itself. The size of a rain droplet varies with climatic conditions, however, it typically varies between 0.5 and 5mm in diameter. Above this diameter, they become unstable and can fragment into multiple smaller rain droplets. In 1950, Best [4] proposed an equation for probability density functions (PDF) for raindrop sizes dependent on rain intensity. An example of these PDFs is shown in Figure 2.2

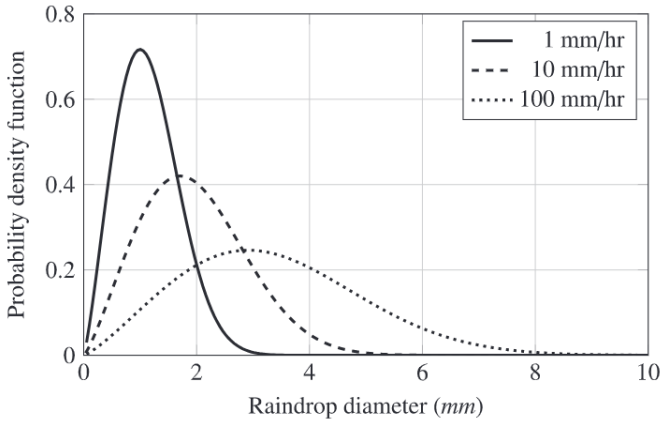

Figure 2.2: Probability density functions of drop sizes for different rain intensities, from [2].

The impact velocity of the blade and the rain droplet is dependent on both the speed of the blade and the speed of the rain droplet. The terminal velocity of a rain droplet is dependent on its size, as its frontal area scales quadratic with its diameter, while its mass scales to the third power. Gunn and Kinzer [12] studied the terminal velocities for rain droplets in stagnant air and found the relationship shown in Figure 2.3A simple vector addition shows that, since the droplet speed is much lower than the tip speed, even during a blade's downward motion, the resulting impact speed does not drop below 80m/s for a tip speed of 90m/s. Similarly, during the upward motion of the blade, the impact speed reaches values up to 100m/s.

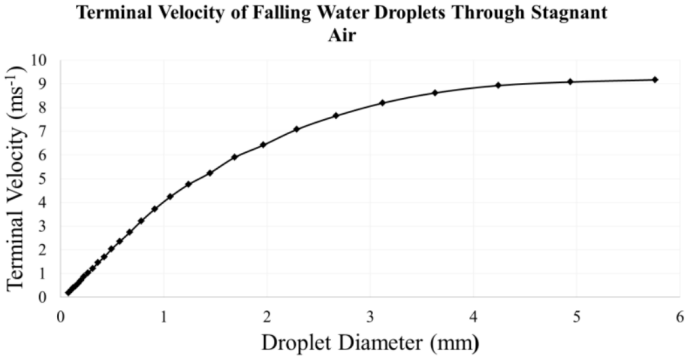

Figure 2.3: Terminal velocities for different sized rain droplets,from [24].

2.3. Impact mechanics

When such an impact occurs, multiple things take place. First, when the droplet impacts a solid surface, the stagnation of the droplet results in the so-called water hammer pressure, first described by Cook [29] as:

$$P = \rho_L C_L V \cos(\theta) \tag{2.1}$$

Where ρ_L, C_L, V and θ are the density of the liquid, the speed of sound in the liquid, the impact speed of the droplet, and the droplet impact angle. Cooks equation follows from the conversion of the kinetic energy of the droplet into elastic potential energy inside the droplet. However it ignores the effect of shock waves in the solid material. Springer [28] includes this effect using:

$$P = \frac{\rho_L C_L V}{1 + \rho_L C_L / \rho_s C_s} \cos(\theta) \tag{2.2}$$

Here the subscript L denotes the liquid and s the variables for the solid. One can see that a lower impedance $(C\rho)$ of the solid results in a lower water hammer pressure and, thus, lower impact stresses. When the impedance of the solid is much higher than the impedance of the liquid, equation 2.2 reduces to equation 2.1.

However, the impact of a rain droplet is not a static event, so the contact pressure will vary with time and location. An approximation for the peak impact stress was found by Heymann [18]:

$$P = 3\rho_L C_L V \cos(\theta) \tag{2.3}$$

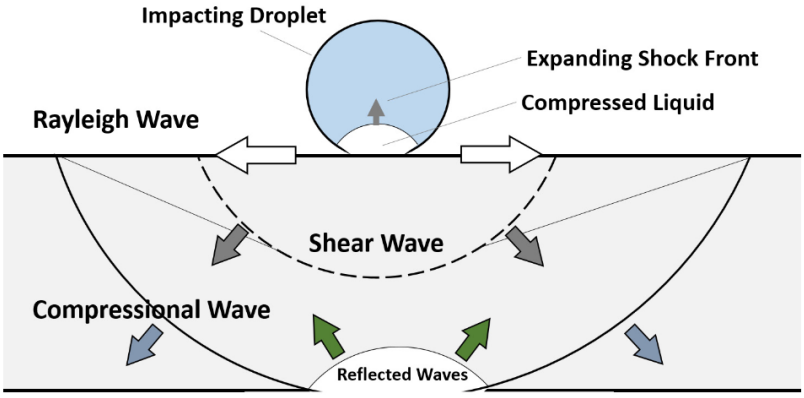

Figure 2.4: Droplet impact and pressure waves, from [22]

In all these equations it is assumed that only the orthogonal velocity component of the droplet results in impact pressure. A study from [42] suggests that the change in impact pressure is even larger. In their study, the maximum contact force of a rain droplet decreased from $75N$ to $18N$, under a $90°$ and $30°$ angle, while the cosine would suggest only a 50% decrease to 37.5N. This is because Springer assumes that the only effect the impact angle has is that only the orthogonal velocity component plays a role. In reality the droplet no longer contacts the surface head-on, instead its impact is partially from the side. This results in a more gradual build-up of pressure compared to the instant water hammer effect, reducing the water hammer pressure.

2.3.1. Formation of stress waves after impact

As a result of the impact pressure, stress waves form in the solid. They can be subdivided into compression waves travelling inwards, shock waves travelling transversely within the solid, and Rayleigh waves travelling on the surface of the solid. Stress waves can cause fatigue cracks, interact with microstructures, or lead to the delimitation of the coating. Therefore, the propagation of stress waves is considered one of the main reasons for coating failure.

2.3.2. Lateral jetting

During the water hammer effect, a compression wave forms inside the water droplet. As this wave travels further into the droplet, it reaches the bottom edges of the droplet as shown in Figure 2.5. At this point, the energy in the wave is released as lateral outflow. This phenomenon is called lateral jetting. The velocity of the lateral jetting can be 2 to 5 times larger than the impact velocity. [5] Thomas and Brunton [30] found that these jets have only a small erosive impact on polished surfaces but a large effect on rough surfaces. They used a tangential jet at 350m/s on a copper surface. For the polished

surface there was hardly any damage, however for the surface with pits of a few microns deep, large amounts of erosion damage were found. This indicates that once a surface becomes lightly damaged from repeated impact, lateral jetting will play a large role in the damage progression, while it is not responsible for the initial damage.

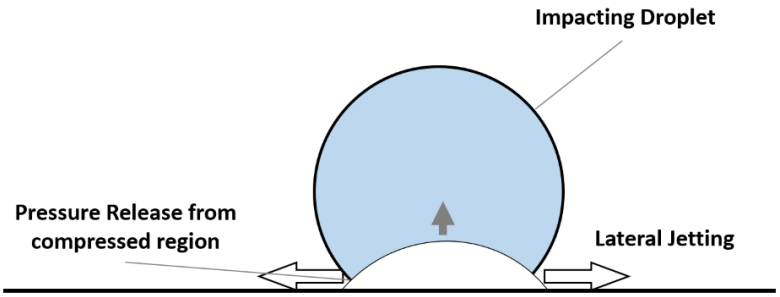

Figure 2.5: Lateral jetting, from [22]

2.3.3. Damage mechanisms

While it is known what happens during the impact of a single droplet, it is less clear what components of the impact actually cause the erosion of the protective layers and heavily depend on materials and conditions. It is likely that one or more of the mechanisms discussed below play a significant role.

As discussed above, the lateral jetting tearing into irregularities and previously formed pits from the impact or fatigue cracks can play a large role in erosion damage. However, since lateral jetting is only damaging rough surfaces, another damage mechanism first has to be present before lateral jetting can have a significant impact. While a single droplet impact is usually not enough to cause damage to the material, repeated impacts and its stress waves can lead to fatigue cracks on the surface. These cracks are locations where the lateral jetting can erode the surface away. Another damage mechanism is the delamination of protective coatings due to the internal stress waves. Since there is often a mismatch in stiffness between the coating and composite, stress concentrations occur at the interface which leads to delamination.

In conclusion, erosion typically consists of three phases: the incubation stage, the steady-state erosion rate, and the final erosion stage. During the incubation stage, damage starts to occur in the material due to the repeating impacts, however no mass loss has yet occurred. When the damages become larger, pieces of coating start to be eroded away, this is the steady state erosion where the mass loss is linear to the number of droplet impacts. Once the material is heavily damaged, the additional damage starts to become more random, this is called the final erosion stage. The erosion stages are visualized in Figure 2.6

2.3.4. Springer model

To model this erosion behaviour, Springer derived a model, using his expression for the water hammer pressure from Equation 2.2. His model computes the lifetime based on a fatigue model. For most materials, this model of the so-called fatigue strength (S) can be sufficiently approximated by:

$$S \approxeq \frac{4\sigma_U(b-1)}{1-2\nu} \tag{2.4}$$

Where σ_U is the material's ultimate strength, ν is the Poisson's ratio, and b is the "fatigue knee" parameter, dependent on the endurance limit (σ_1), σ_U and a constant b_1.

The number of impacts until incubation for a single site, i.e. the area the same size as the cross-sectional area of a droplet, can be described by:

$$n_i^* = a_1 \left(\frac{S}{P}\right)^{a_2} \tag{2.5}$$

Springer fitted experimental rain erosion test data to this equation and found a value of $7.0e-6$ for a_1 and a value of 5.7 for a_2. If one wants to know the number of impacts per square meter (n_i), Equation 2.5 can then be rewritten as Equation 2.6 with d being the droplet diameter in mm.

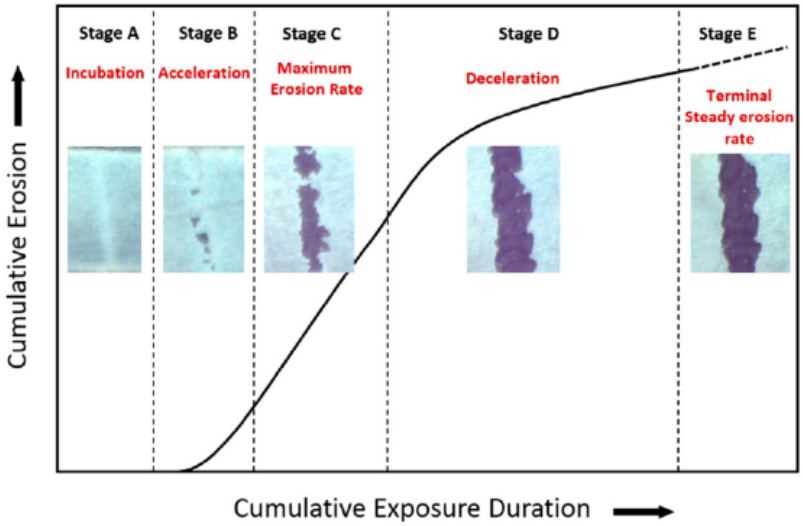

Figure 2.6: Accumulative erosion vs. time, from [22]

$$n_i = \frac{8.9}{d^2}\left(\frac{S}{P}\right)^{5.7} \text{ impacts/m}^2 \tag{2.6}$$

Since this is only a model for a homogeneous material, it is not fully valid for a coated material. Springer also extended this model to include coated substrates. However, since the model presented here is simple, it provides a good way to understand the approximate impact which various parameters may have on the incubation time. For example, a 13% increase in impact pressure results in halving the incubation time.

Coated substrate

Springer also extended his model to a coated substrate. This model uses a coated layer with a finite thickness and takes 1D wave propagation within the coating into account, i.e. the compressional wave from Figure 2.4. Including this complicates the model to where the stress in the coating P_c now becomes:

$$P_c = P\frac{1+\psi_{sc}}{1-\psi_{sc}\psi_{lc}}\left[1-\psi_{sc}\frac{1+\psi_{lc}}{1+\psi_{sc}}\frac{1-e^{-\gamma}}{\gamma}\right] \tag{2.7}$$

Where P is the water hammer pressure from Equation 2.2 used with the material properties of the coating. ψ_{lc} and ψ_{sc} are Impedance parameters for the liquid-coating interface and the liquid-structure interface respectively. γ is the coating thickness parameter.

The fatigue strength from equation 2.4 for the coated substrate is also changed to:

$$S_c \approx \frac{4\left(b_c-1\right)\sigma_{u,c}}{\left(1-2v_c\right)\left(2k\left|\psi_{sc}\right|+1\right)} \tag{2.8}$$

As one can see this coated model is already significantly more complex compared to the uncoated model. Hoksbergen et al. [20] found in a large sensitivity study on the coated Springer model that the coated Springer model is very powerful and computationally friendly due to its analytical nature. However, it showed that for materials with a Poisson ratio close to 0.5, the model predicted extraordinarily high coating performance. Moreover, it was also sensitive to changes in ultimate tensile strength and fatigue limits around this point. This means that here the model is not reliable and should be used with caution, especially as the Poisson ratio of many modern elastomers, which are used as coatings, possess a Poison ratio close to this value of 0.5.

2.3.5. Layer thickness

Based on their conclusions of the limitations of the Springer model for modern elastomers, Hoksbergen et al [19] decided to further study the lifetime performance of coated substrate using numerical methods. One of the parameters they studied was the coating thickness in relation to the droplet diameter. The results are shown in Figure 2.7. As one can see, for the smallest droplet diameter there is hardly any difference between the various coating thicknesses, while for the larger droplet diameters, the difference can be as much as an order of magnitude between the different coating thicknesses. This indicates that the incubation time is highly dependent on the coating thickness until a certain thickness is reached, after which it behaves similarly to a bulk material. Where this transition point is depends on the coating material and droplet diameter.

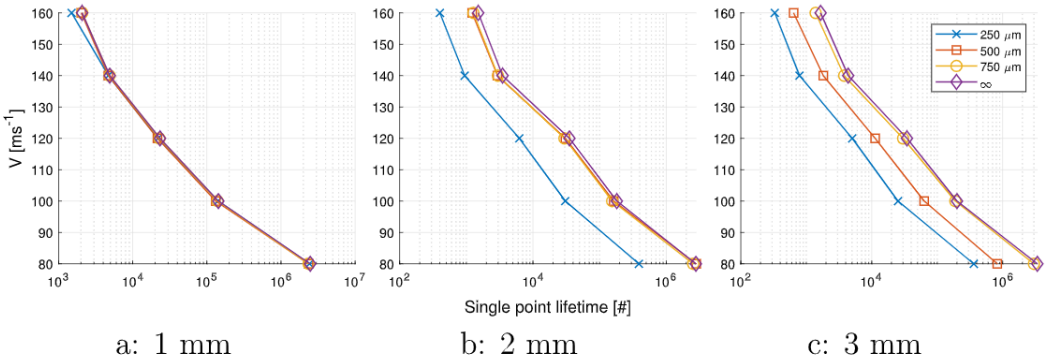

Figure 2.7: "The effect of LEP thickness on the predicted lifetime of PAI coated epoxy substrates for different droplet diameter impacts at a single location." From: [19]

2.3.6. Non-flat surfaces

The vast majority of research on leading edge erosion has focused on the impact on a flat sample, which is accepted as a reasonable simplification of the curved leading edge. Research into erosion on curved surfaces has been done by among others, Burson-Thomas et al. [6], Verma et al. [33]. and Wu et al. [36]. They all found that the impact forces were lower and shorter in duration for a convex surface compared to a concave surface. This is caused by the shock wave from the water hammer pressure reaching the outside of the droplet earlier, starting the lateral jetting stage. This is shown in Figure 2.8. The research also showed that this effect increases as the ratio of droplet radius r and surface radius R gets smaller. The study of Burson-Thomas et al. had the smallest ratio of R/r = 1, as their scope of research was droplets hitting the leading edge of fan blades in turbines. They found that both the maximum contact radius and time during which there is a shock front are halved compared to a flat surface. This would lead to a significant lower erosion rate. A recent experimental study by Fujisawa and Aihara [11] however found that the erosion rate of aluminium cylinders undergoing liquid impact rose significantly when r/R increased from 0.02 to 0.13. This is directly in contrast to the expectations from the earlier theoretical studies. A possible explanation for this is given by Fujisawa and Aihara. Their simulations showed that due to gravity the water cushion that forms on a flat surface was thinner and reduced in thickness faster for the curved surface. This reduced water cushion effect could explain why more erosion was observed for the curved surfaces.

All research found focused on a ratio of r/R $\geq$ 1 for the convex surfaces. No work has been found for r/R < 1. Similarly not much information on concave surface impact has been found, the only information was in the work of Wu et al. [36]. In their study, they focused on a concave surface with a ratio of r/R = 1. As can be seen in Figure 2.8, there is a large contact area resulting in a large and longer continuing shock wave, resulting in more erosion. However, no information has again been found or ratios of r/R < 1, which is a very different case, as there will be two simultaneous contact points on both sides of the droplet. This has thus been identified as a gap in the current knowledge of high-speed droplet impact mechanisms.

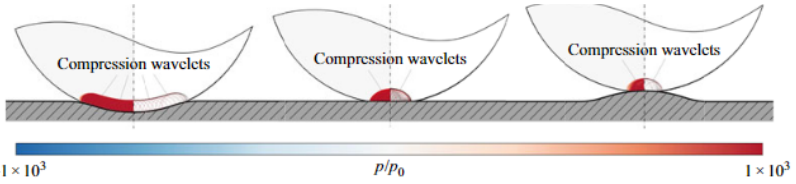

Figure 2.8: Size of shock wave in droplet for concave, flat and convex surface, from [36]

2.3.7. Numerical modeling

Since the impact mechanics are very complex, significant research has gone into numerical simulation of the impact mechanics and the resulting material failure. Different models have been developed for different scales. Lifetime prediction of a wind coating for site-specific circumstances requires, for example, a different kind of model compared to studying the details of impact mechanics. One such model to study the lifetime of the coating based on site and wind turbine conditions has been made by Verma et al. [34]. However, in this thesis, the focus is more on the study of the behaviour of the structuring of coatings and not on predicting the coating lifetime in a site. Therefore, a different kind of model is required. One that accurately models the stresses the sample experiences and one that can work with the large deformations a droplet hitting a structured surface experiences.

According to Chen et al.[8] several different methodologies for modeling high speed impacts exists:

- Standard finite element method (FEM) techniques using a Lagrangian meshing method. This method is widely used, however as it consists of a predefined mesh, it is limited to situations with relatively limited deformation.
- A combination of a Lagrangian mesh for the sample and an Eulerian mesh for the droplet. The advantage is that this is less sensitive to deformations, however it is very computationally intensive.
- A combination of a Lagrangian FEM model for the sample and smoothed particle hydrodynamics (SPH) for the droplet model. Instead of modelling the droplet using a mesh, SPH models it using particles. Each particle has a mass and can represent the hydrodynamic (pressure, velocity) and thermodynamic (temperature, phase changes) state of the fluid. The particles and their properties are connected using an interpolation function. This function describes how the properties of a particle interact with the properties of its neighbouring particles. The advantage of this method is that since there is no computational mesh, it is suitable for large deformations and is highly computationally efficient. This kind of SPH model for liquid droplet impact has been developed at TU Delft by Verma et al. [35]. They first developed a simple model of a droplet hitting an aluminium plate and compared the results to experimental results from Zhang et al. [40]. The numerical results agreed within 2.1% with the experimental results. Based on this, a more complex model, including several layers of GFRP and a gel coat, was made. This model was then used to analyse impact forces, stresses and strains in the sample in a parametric study.

2.3.8. Theory behind SPH

To get a better understanding of what happens in an SPH simulation, the theory behind an SPH model will be discussed below. As explained above, a SPH model consists of multiple particles. As these particles together represent a continuous material, i.e. the water droplet, they are a discretization of a continuous field. Thus each particle is an approximation of the field values of the area around it. This approximation $u(\boldsymbol{x})$ is called a kernel smoothing function and is described as:

$$u(\boldsymbol{x}) = \int_{\Omega} u\left(\boldsymbol{x}'\right) W\left(\boldsymbol{x} - \boldsymbol{x}', h\right) d\boldsymbol{x}' \tag{2.9}$$

In this equation, W is the smoothing function which describes how much the values of the field around it influence $u(\boldsymbol{x})$ as a function of the distance to $\boldsymbol{x}$. Ω is the domain wherein the smoothing function acts. The smoothing function that is used most often, and also in the research of Verma et al.,

is the B spline function:

$$W\left(\boldsymbol{x}-\boldsymbol{x}',h\right)=\frac{C}{h^d}\times\begin{cases}1-\frac{3}{2}\xi^2+\frac{3\xi^3}{4}, & 0\leq\xi<1\\ \frac{1}{4}(2-\xi)^3, & 1\leq\xi<2\\ 0, & \xi\geq 2\end{cases} \tag{2.10}$$

Where h is the smoothing length, i.e. the distance that defines how far away from the point $\boldsymbol{x}$ the smoothing function is acting. C is a constant based on the space dimensions. ξ is the distance between particles $\boldsymbol{x}$ and $\boldsymbol{x}'$ defined as $\frac{|\boldsymbol{x}-\boldsymbol{x}'|}{h}$.

Since Equation 2.9 is a continuous function, it has to be discretized to be able to be used with the discrete particles in SPH. The integral now becomes a sum of the particles within the area. For the particle i at location x_i the function can now be represented as:

$$u\left(\boldsymbol{x}_i\right)=\sum_{j=1}^{N}\frac{m_j}{\rho_j}u\left(\boldsymbol{x}_j\right)W\left(\boldsymbol{x}_i-\boldsymbol{x}_j,h\right) \tag{2.11}$$

Where N is the total number of particles within the smoothing area of i. This number of particles is determined by the smoothing length h multiplied by a scalar constant κ. m_j and ρ_j are the mass and density of the particles. Figure 2.9 shows a schematic approximation of the kernel function.

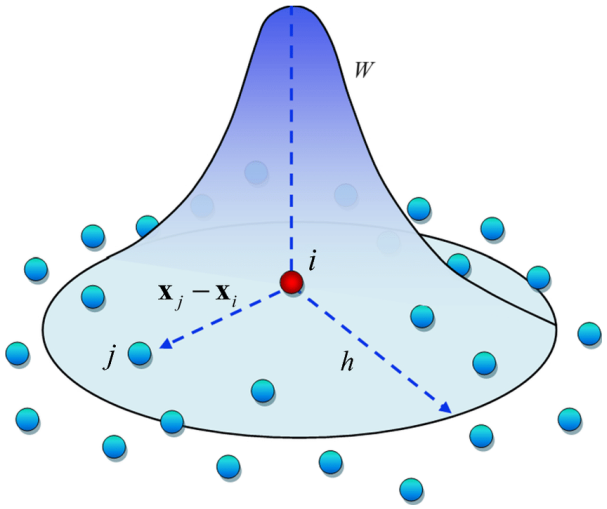

Figure 2.9: Schematic representation of the kernel function W acting on a particle i, with a smoothing length h. Adapted from: [3]

2.4. Testing

There are many different test methods for characterizing materials' resistance to rain erosion. Two of these methods will be discussed below. One is the whirling arm tester, which is often used to characterize commercially available materials. The other is the pulsating jet erosion tester, which is available at TU Delft.

2.4.1. Whirling arm tester

Several test methods have been developed to characterise rain erosion. One is the rotating jet erosion tester, which consists of a rotating arm with scale models of a wind turbine's leading edge mounted to it. This arm rotates through a curtain of falling rain droplets, imitating real-world conditions. Rotating arm erosion testers are the state of the art in erosion testing; however, they are expensive to buy and operate.

2.4.2. Pulsating jet erosion tester (PJET)

Another type of erosion tester is the pulsating jet erosion tester (PJET). It uses a stationary sample and a water jet, which is interrupted by a spinning disc with one or multiple holes. The PJET can

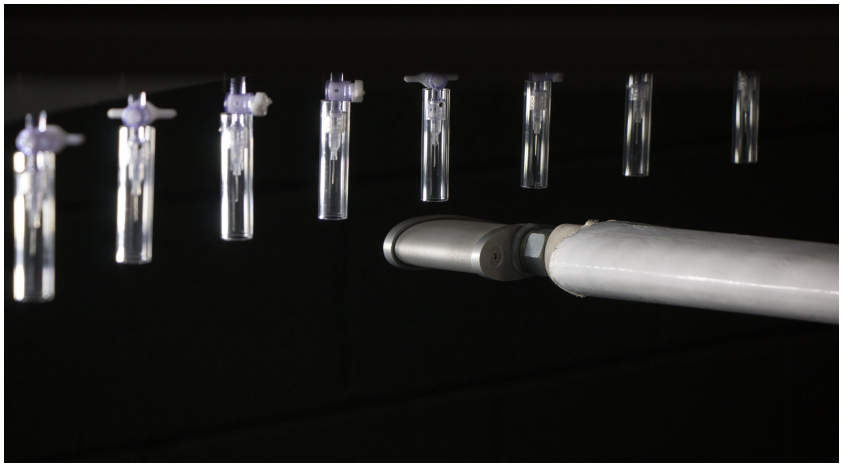

Figure 2.10: Whirling arm erosion tester, from [10]

spray droplets at a range of speeds and frequencies, making it useful for characterizing materials more cheaply than the rotating arm tester.

In PJET testing, there are multiple ways of defining erosion. A very common method is incubation time, which is defined as the time or number of impacts until the first visible damage occurs. Another method is, after incubation time, to measure the mass or volume loss rate. The downside of the volume loss rate is that it is difficult and takes a lot of time to measure correctly. This is because the sample has to be removed from the PJET and dried, every time a measurement needs to be done. For this reason, the time until the first visible damage is taken as the quantification of erosion resistance.

A drawback of the PJET method is that the droplets are not real droplets but more chopped-up water jets, with a theoretical length of:

$$L_{droplet} = \frac{V_{jet}}{\alpha\omega} \tag{2.12}$$

Where $L_{droplet}$ is the length of the droplet, V_{jet} is the velocity of the jet, α is the opening angle in the disc and ω is the rotational speed of the disc. As a result, the droplet length, impact frequency and impact velocity can not all three be separately controlled, setting two parameters dictates the third one. For example, a 160m/s jet with a rotational velocity of 47.5Hz, results in a droplet length of 10cm.

Another side effect of using the impacting jet without high-speed air moving over the sample is the formation of the water cushion effect. This is explained in previous research by Alonso Diaz[1], which suggests that a water film can stay behind on the sample between impacts, which results in less damage due to forming a cushion. However, using either an air blast at the impact location or a lower impact frequency would eliminate this effect. Another conclusion from Alonso Diaz's research was that the results were very sensitive to the temperature and humidity of the sample and the water. For this reason, it is very important to heat up the machine properly before starting tests.

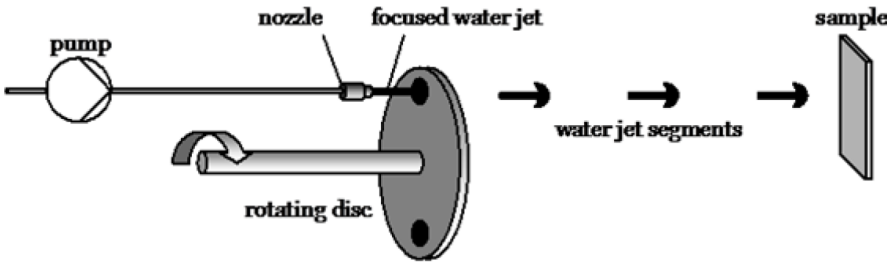

Figure 2.11: Jet impact tester, from DUCOM [9]

2.5. Current solutions

To increase the erosion resistance of the leading edge, numerous means of protection have been developed. Typically a coating is used that protects the expensive composite blade from erosion damage. There are typically two categories of coatings. The first is the polyester or epoxy gelcoat. This coating is applied in-mould during the blade's manufacturing. Because it cures together with the blade, its properties have to be similar to those of the blade composite material. The gelcoat cures typically to a very hard material and thus resists erosion.

A more modern coating material is the polyurethane (PU) coating. This is a coating that is applied post-mould. Contrary to the gelcoats, a PU coating is very flexible and has good erosion and impact resistance due to being able to dissipate the impact energy. The comparison of a gelcoat and a polyurethane coating can be seen in Figure 2.12. The thickness of a PU coating has a large impact on its performance. The typical thickness of a coating is in the order of 0.3-1mm.

An alternative to spraying the polyurethane coatings is the application of polyurethane tapes. The material is similar to the spray coating but is now a thin sheet that can be applied to the leading edge using an adhesive. This is a good option when erosion has already been observed and is easier to retrofit on-site compared to painting the leading edge.

Although all these solutions provide significant improvement over an uncoated blade, maintenance is still required relatively often, as indicated by Keegan et al. [24]. Therefore, improvements to the erosion resistance would significantly decrease the operational costs of wind turbines.

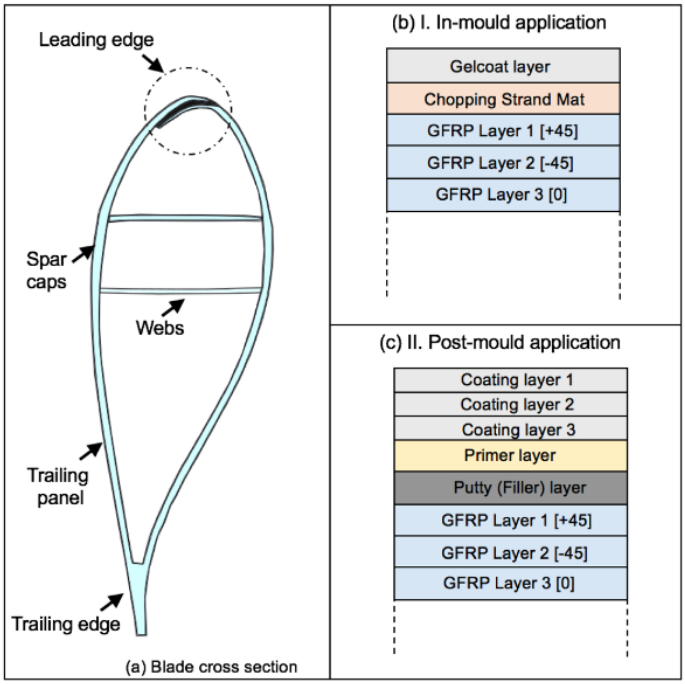

Figure 2.12: A typical blade construction (a), in-mould coating application (b), and post-mould coating application (c), from [35]

2.6. Erosion resistance in nature

Not only wind turbines undergo erosion. A lot of things on earth undergo erosion through, for example, flowing water or sand storms. Evolution has led to some organisms being very erosion-resistant. Examples of this are, for example, sea shells which deal with wear due to the moving soil. Three different types of mollusc shells were studied by Tong et al. [31], and they found that the wear resistance significantly depended on the orientation of the shell ridges to the soil movement direction. Other organisms that have been studied are, for example, the dung beetle, ground beetle, centipede and the mole cricket [32]. The morphology of these organisms consists of either corrugated surfaces with ridges or dimpled surfaces which have either convex or concave domes.

While soil erosion is different from liquid droplet erosion, no organisms subject to liquid droplet erosion have been identified. An erosion process that has similarities to liquid droplet erosion is sand

erosion. Sand storms also can have relatively high speeds, resulting in high kinetic energy impacts. However, the behaviour of materials is different when impacted by a solid particle compared to the behaviour of water droplet impact, which was discussed before.

Jung et al. [23] studied the behaviour of a material subject to solid particle impingement. They found that for low impact angles, the particle cuts a piece of the material as is schematically shown in Figure 2.13a. As the impact angle increases, the dominant erosion mechanism changes from cutting to plastic deformation and brittle fracture, as shown in Figure 2.13b and 2.13c. They found that the erosion rate at an angle of 20° is 3.4 times higher than the lowest erosion rate at 90°. This is different from water droplet erosion, where the maximum erosion rate is at an impact angle of 90°.

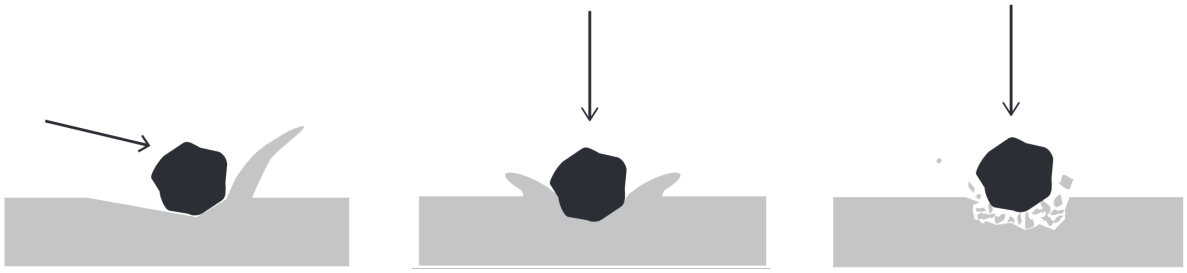

(a) Cutting action **(b)** Plastic deformation **(c)** Brittle fracture

Figure 2.13: Erosion mechanism for solid particle impingement for different impact angles, from [23]

Multiple organisms are subject to this particle-laden flow erosion. A place where this occurs is in desert sand storms. A sandstorm in the desert consists of suspended particles in the air. Sand is classified as particles between 0.05mm and 2mm in diameter. However particles above 500um very quickly fall down and are thus not suspended in the air, and particles above 100um are only present in the lower 1,5m part of the air.

The organisms subject to these sand storms all possess mechanisms to withstand this type of erosion. Examples of these organisms are the desert scorpion, the desert lizard and the tamarisk tree. Their anti-erosion characteristics are comprised of multiple different mechanisms. Firstly the materials are able to withstand erosion well. Zhang et al. [38] and Han et al. [13] found that the carapace of the desert scorpion consists of multiple smaller hard sections coupled by a larger elastic tissue. Similarly, Huang et al. [21] found that the skin of the desert lizard consists of hard scales coupled by a soft layer. In both organisms, the hard shell protects against direct impact damage, while the softer tissue dissipates the impact energy. Han. et al. [16] found that the wood of the tamarisk tree had a higher modulus of elasticity and hardness at the windward side compared to the leeward side. In addition to this, the rings of the tamarisk grow eccentric, with a higher cell division rate towards the windward side, resulting in more material.

In addition to these tailored materials, the surface morphology of these organisms also plays an important role in the erosion resistance of the organisms. Zhiwu et al. [41], Zhang et al. [38][39], and Han et al. [13] all found grooves and domes on the surface of the scorpion's carapace, as can be seen in Figure 2.14. The grooves have a size of 0.5-1mm. The grooves and domes are believed to work using two mechanisms. The first is by changing the local impact angle. Since lower impact angles result in more erosion, locally increasing the impact angle helps to reduce erosion. This change in impact angle is shown in Figure 2.15a. The second mechanism is the creation of vortices by the wind blowing over the ridges, these vortices then alter or slow down the trajectory of the impacting particles. A schematic overview of this is shown in figure 2.15b. Similarly to the desert scorpion, Han et al.[16][37] found that the bask of the tamarisk also had grooves and domes, as is shown in figure 2.16. The groove sizes were <3mm and the dome sizes were roughly 0.5-1mm.

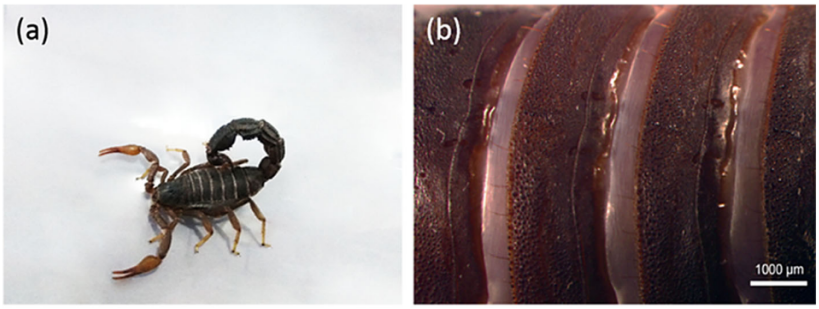

Figure 2.14: Desert scorpion and its carapace, from [39]

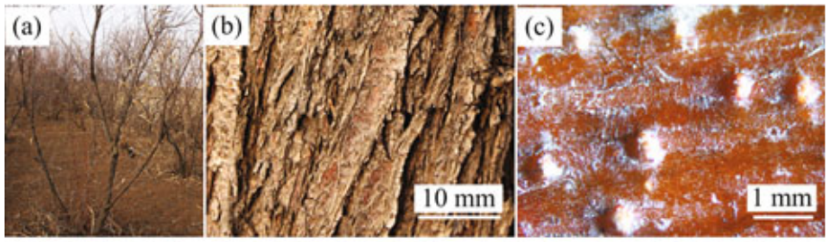

Figure 2.16: a) Tamarisk b)bark c)grooves and domes on bark, from [16]

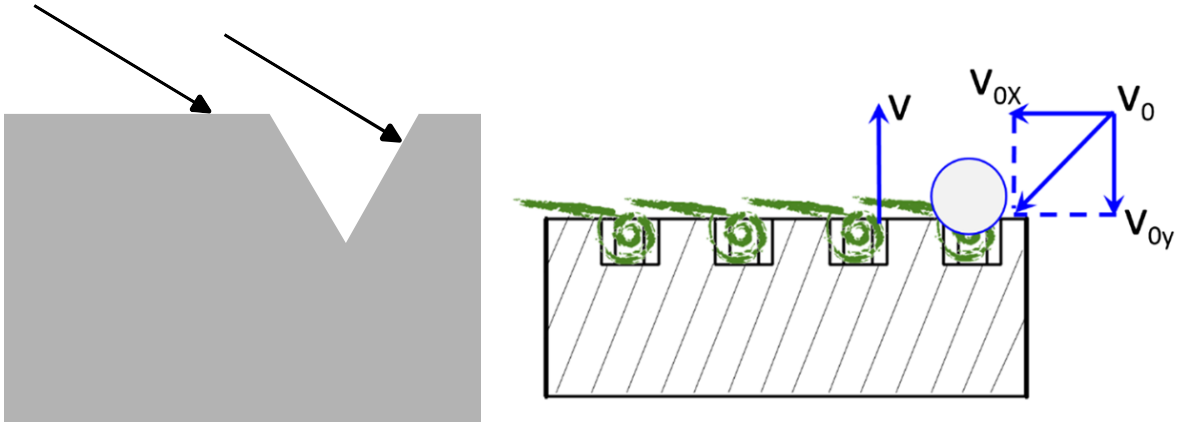

(a) Increasing local impact angle

(b) Vortex generation, from [39]

Figure 2.15: Two mechanisms of reducing impact

2.6.1. Biomimetic design

The erosion resistance of the aforementioned organisms was not just studied to understand how they worked. The goal for most of these studies was to understand underlying mechanisms so they could be applied to engineering problems. This is called bionics. For example, Zhang et al. [39], and Zhiwu et al. [41] developed surfaces that also consisted of grooves and domes. Similarly, Yin et al. [37] also developed a structure with grooves based on the tamarisk. There are also other, non-erosion related, surfaces being developed. For example, a gecko-inspired dry adhesive based on the gecko's skin morphology. Another example is the use of shark-skin inspired features on swim suits, which reduce drag.[15] When looking at how these features are designed, they all do essentially the same thing. First, an understanding of the working mechanism is obtained, then it is scaled to the problem at hand and tried to be replicated in its simplest form possible in order to be easily manufacturable. While nature often forms very organic, complicated shapes, our manufacturing methods usually favour simple, geometric shapes.

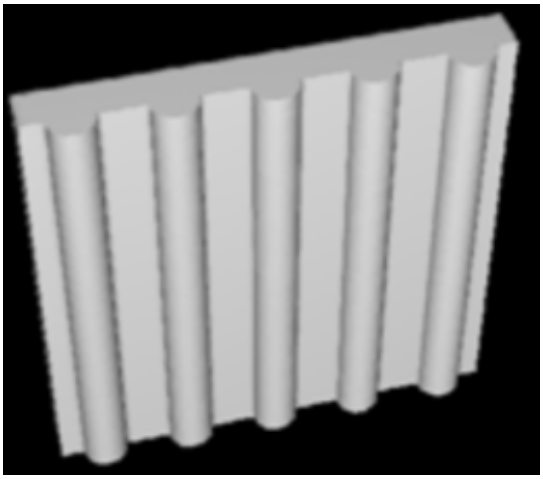

(a) Scorpion inspired surface, from [38]

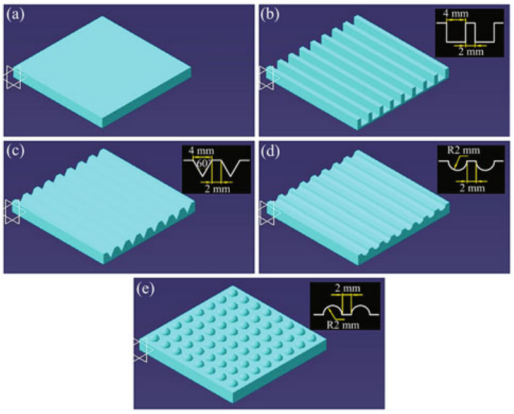

(b) Tamarisk inspired surfaces, from [16]

Figure 2.17: Desert scorpion and tamarisk inspired surfaces

3

Methodology

Both numerical and experimental methods are available to answer the research questions. Both have different strengths and weaknesses. Numerical methods are suitable for studying what happens during a droplet impact. However, the mechanisms leading to the failure of the material coating are complex, and this failure is difficult to capture accurately using simulations. For this reason, it was decided to combine both methods to answer the research questions. The following section will focus on the experimental approach, after which the numerical approach will be discussed.

3.1. Experimental approach

A PJET tester is available at TU Delft to perform experiments on rain erosion. To get representative results using this tester, it is essential that the sample is a good representation of a leading edge and that it changes as few variables as possible. For a typical test in the PJET tester, a flat glass fibre-reinforced plastic (GFRP) plate with the coating adhered to it for testing is often used. Changing as few variables as possible ensures comparable results between experiments. Therefore, it is chosen to keep the layer thickness identical over the entire sample area. This is done to reduce the effect of wave propagation in the various samples. The implication of this constant layer thickness is that the substrate must follow the contours of the sample. Since this is impractical to do with GRFP, a substrate material that is sufficiently stiff enough for the results to be comparable to a GRFP substrate must be selected. For this study, a substrate consisting of 100% epoxy has been chosen as a substrate material. While it is less stiff than GRFP, it is still multiple orders of magnitude stiffer than the polyurethane and thus should be sufficient. The advantage of this material is that it can be cast into a mould before curing, making it easy to obtain irregularly shaped samples. As was defined in the research question, triangular-shaped features will be used on the sample. These triangular shapes were chosen since these are the simplest possible geometry. Since there is not much knowledge available on using these geometries, a simple geometry provides the highest chance of gaining knowledge as there are fewer possible complications and interactions due to the chosen geometry, leading to a higher chance of gaining new insights. A sketch of such a sample is shown in Figure 3.1.

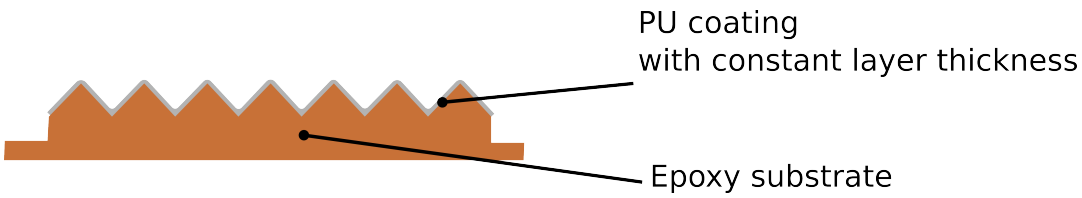

Figure 3.1: The epoxy substrate with a constant layer thickness coating

The samples will have an approximate size of 80x80mm, as this is deemed large enough to perform all required tests on a single sample, while larger dimensions would result in more work than needed. A smaller sample would not be able to fit the largest features. The feature angle, height, and spacing will

be tested with three different values to answer the sub-questions. Only one variable will be changed at a time. The definition of feature angle, feature height and spacing are shown in Figure 3.2.

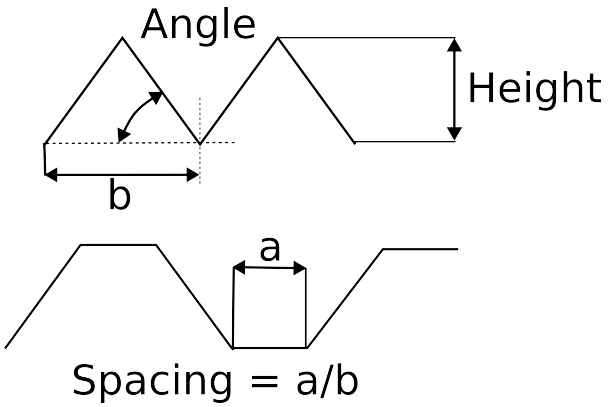

Figure 3.2: Illustration of parameters used for the samples

3.1.1. Impact angle

When the angle of the grooves is changed, the impact angle at which the rain droplet impacts the material is also changed. A larger impact angle will result in less impact force, while a smaller impact angle will result in the largest impact force. At an angle of 0°, i.e. a flat surface, the impact forces are at maximum. This suggests to use a large angle for the grooves. However, a large groove will likely be fragile, and more grooves are needed to cover the same width for the same height. For this reason, it is interesting to test different angles. The chosen angles are 20°, 40° and 60°. 20° is chosen as the smallest angle because an even smaller angle will result in wide grooves for the same height, which is impossible to test efficiently with the erosion tester. An angle larger than 60° is also not used because it is expected to be too fragile. These chosen angles do not directly relate to the feature angles of the organisms. This is done because the mechanism behind the change in erosion resistance due to the angle is different for solid particles and liquid droplets, as was explained in Section 2.6.

3.1.2. Sample height

Inspiration is taken from erosion-resistant organisms, namely the desert scorpion and Tamarisk, to find appropriate sizes for the sample size. As was mentioned in Section 2.6, they have the following groove sizes:

- grooves in scorpion: 0.5 – 1mm
- Grooves in Tamarisk: <3mm
- Domes on Tamarisk: 0.1 – 0.4mm
- Sand particle size: 0.05 – 0.5mm

The above leads to the conclusion that the features are roughly 1-10x the size of the erodents. For a standard rain droplet of 2mm, this would result in a feature size of 2 – 20mm. However, because of the limited sample size that fits the test setup, the feature size is capped at 10mm. The chosen feature sizes are 2, 5, and 10mm.

3.1.3. Spacing

In nature, the grooves are often not spaced directly near each other; there is some spacing between them. For this study, spacing is chosen to involve both the spacing at the top and in the valley because extra damage is expected to occur in both locations. In nature, the spacing between the samples is roughly 0.5-1x the sample height. Spacings of 0x, 0.5x, 1x will be used to test this. This will be tested for just a single height/angle combination to reduce the number of samples required. It will be tested both for the top spacing, i.e. forming grooves and for the bottom spacing, i.e. forming bumps. Table 3.1 shows the eight resulting geometries.

Angle [°]	Height [mm]	Spacing [-]
0	0	0
40	5	0
40	2	0
40	10	0
20	5	0
60	5	0
40	5	0.5
40	5	1

Table 3.1: The eight different samples used

3.2. Sample preparation

The samples consist of an epoxy substrate covered with a $300\,\mu m$ thick layer of a PU erosion-resistant coating.

3.2.1. Substrate

The substrate is made from Scabro 1200 epoxy with 60% 1204 and 40% 1208 hardener. A mould is required to make the substrate. The mould is made by FDM printing the shape of the substrate from PLA. This shape is then sandblasted to reduce the layer line effect. Afterwards, a silicone mould is cast using Silastic S green silicone. The final substrate can be made using this mould. Before casting, the epoxy is outgassed for 20 minutes in a vacuum chamber. When the epoxy is in the mould, it is again outgassed for 20 minutes. This is required because it was found that small bubbles would form at the interface between the mould and the epoxy. This is believed to be caused by the surface not being perfectly smooth due to the layer lines remaining from the printing process. This rough interface can trap air, resulting in bubbles in the final part. Afterwards, the epoxy is left to cure for at least 24 hours before coating. A schematic of the production process is shown in Figure 3.3

3.2.2. Coating

The LT969FD PU coating from PPG with the LW7290-30 hardener is applied using a pressurised air spray gun with a nozzle size of 2mm at a pressure of 3 bar. The coating is mixed according to the datasheet, in addition, 11% of Mipa V25 thinner is added to increase the atomisation of the paint, which increases the smoothness of the coating. Three coating layers are applied to the substrate with a drying time of 2 hours in between coatings. Afterwards, the coating is left to cure for at least 24 hours before testing begins.

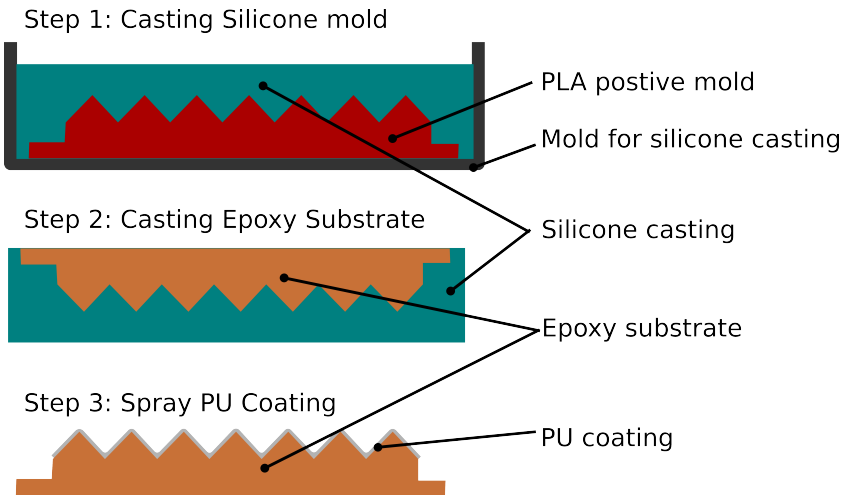

Figure 3.3: Steps needed to produce the samples

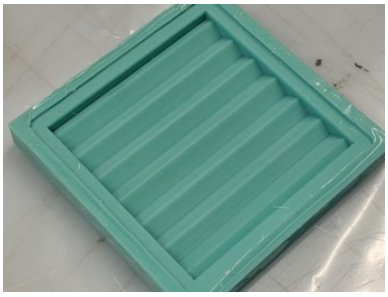

(a) Silicone mould

(b) Epoxy substrate

(c) Coated sample (after testing)

Figure 3.4: Sample production

3.3. Experimental setup

3.3.1. Rain erosion tester

The erosion tests are done using a Ducom liquid droplet erosion tester. It consists of a pump pumping deionised water through a nozzle with a rotating disk that contains a hole. The disk interrupts the jet and thus simulates droplets, as is shown in Figure 2.11. The sample is mounted on a stainless steel plate that can be moved horizontally and vertically to align the jet to a specific location on the sample. To prevent the formation of a water cushion, an air blast is aimed at the impact location. A laser pointer is mounted to the erosion tester so that the impact location can be visualised before turning on the tester. After the water impacts the sample, it is pumped through a radiator to remove most of the heat that originated from the kinetic energy in the high-speed jet. The radiator cannot completely cool the water back to room temperature, meaning that the erosion tester requires a warm-up to get to a stable temperature. This is important because it was previously shown by Alonso Diaz [1] that the temperature greatly influenced the erosion resistance of the material. To observe the damage, a magnetic cleaner, originally meant for fish tanks, is used to wipe away the droplets on the cover. A bright flashlight is used to illuminate the samples to observe damage. An overview of the setup is given in Figure 3.5

The settings used in the PJET tester are shown in Table 3.2. The nozzle diameter of 1.5mm, results in a droplet diameter of 2mm, the most often used diameter in literature, since it is close to the average rain droplet diameter. The pump frequency of 50.5Hz, resulting in a jet speed of 210m/s, is chosen based on preliminary tests on a flat plate. Based on the expectation that the incubation time of the flat surfaces would be orders of magnitude longer. The highest possible speed, which still resulted in typical erosion damage, was selected. The disc frequency of 41.7Hz was selected as this is the highest that the machine will go, thus resulting in the shortest droplets, leading to a result being closer to reality.

Setting	Value
Nozzle diameter	1.5mm
Pump frequency	50.5Hz
Disc frequency	41.7Hz

Table 3.2: Settings used in the PJET tester

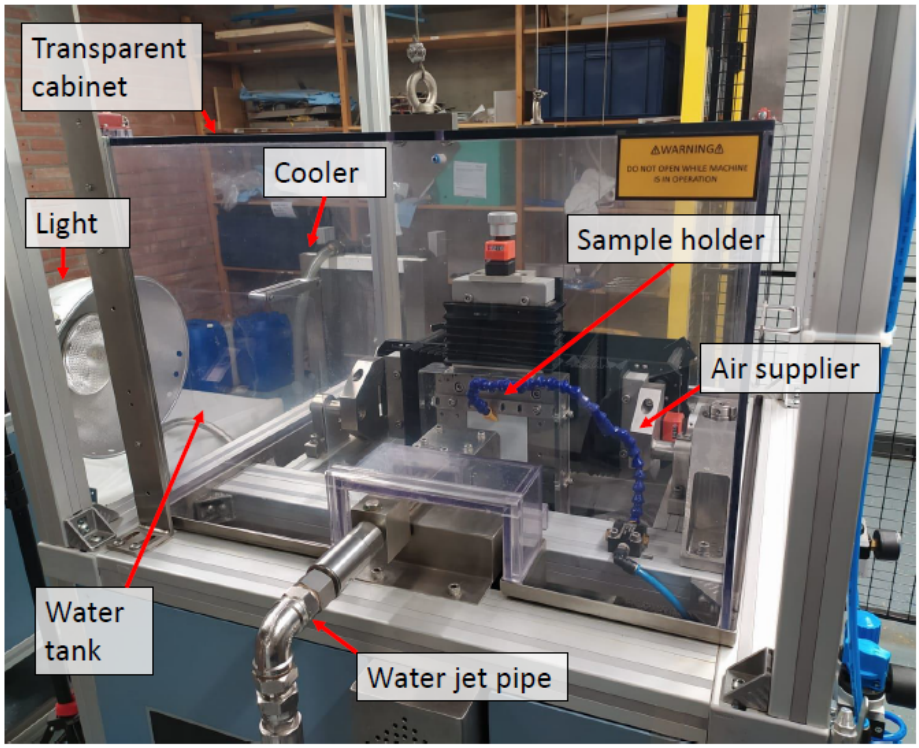

Figure 3.5: An overview of the erosion tester, image from Alonso Diaz [1]

3.3.2. Microscope

The Keyence VK-X3000 confocal microscope is used to inspect the samples after testing. In addition to being a regular optical microscope, it can construct 3d images using either the focus variation or laser confocal technique. The focus variation technique is used here since it is faster than the confocal setting. In addition, the lowest magnification of 2.5x is used because of the longer working distance, which is needed to look in the valley without hitting the top of the features with the objective. However, the working distance is still only 8.5mm, meaning inspecting the valley damages of the 10mm height samples using the microscope is impossible. The microscope is used to study the dimensions of the damaged areas and look at cross-sectional views of the samples cast in epoxy to determine the layer thickness.

3.3.3. High speed camera

A Fastcam mini AX200 monochrome high-speed camera was used to understand better what happens during droplet impact. It can produce 1MP images up to 6400 frames per second (fps) and up to 900.000 fps with a decreased resolution. The images were shot at 20.000fps, and the PJET was set to 50m/s to get enough light and a reasonable resolution. This speed was chosen because it was observed that the jet was not a real jet at lower speeds but more resembled a spray of smaller droplets. The disc rotation speed was also decreased so that the droplet length was equal to the length used during the erosion tests.

3.4. Test plan

3.4.1. Test

Each impact angle sample will be tested at 9 locations: three times in a valley, three times in the middle, and three times at the peak. These locations are shown in Figure 3.6. This ensures sufficient data to detect errors in the measurements. The time and date, as well as ambient and water temperature, will be logged throughout the tests. This is done to see if there is a correlation between results and one of these variables, which could lead to a false interpretation of the results if not discovered.

The process of determining the incubation time using the PJET consists of several steps:

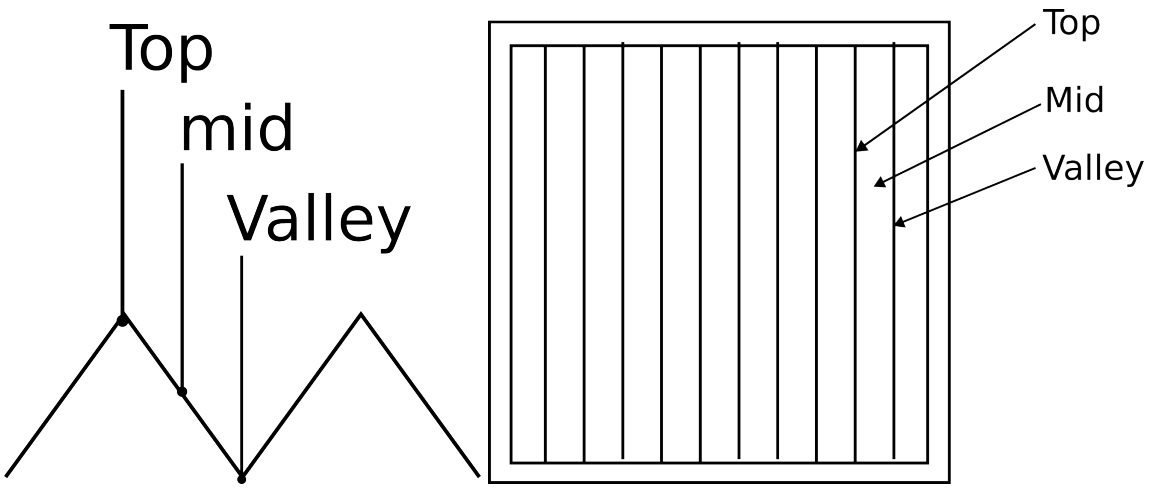

(a) Side view **(b)** Top view

Figure 3.6: The three different impact locations, each location will be tested three times on a sample

1. The samples were placed inside the machine but not mounted in front of the jet. The machine was switched on and was run to heat up for roughly two hours. At that point, the water temperature was around 39° C, which remained stable during the tests.
2. Next, the sample was placed in front of the jet and aimed at the required position. Before the tester was started, the water temperature, environmental temperature, relative humidity and time were recorded.
3. Now, the tester and stopwatch were started. Now, the sample was observed to check for any visible damage. This is done continuously for the first five minutes. Afterwards, this was done in intervals. Hereby, the accuracy of determining the first observable damage is estimated to be 10% with a minimum of 15 seconds.
4. Once damage is observed, the tester and stopwatch are stopped, and the time from the stopwatch is recorded.
5. Next, the sample is moved to the next point, and testing starts again from point 2.

3.4.2. Inspection

After the tests, all samples will be analysed with the confocal microscope to study the damage type qualitatively. In addition to this qualitative study, the dimensions of the damaged area will be measured. In addition, the thickness of the coating on the various samples will be measured. This is done by taking a piece of the sample, embedding it in epoxy, and sanding/grinding until a smooth cross-sectional view of the coating has been achieved. The sample can then be evaluated using the microscope.

3.5. Coupled SPH-FEM simulation

When the experiments were finished and analysed, it was concluded that the results did not provide a complete understanding of the observed phenomena. It was hypothesised that a simulation of a single droplet impact on the different samples would improve the understanding of the mechanisms and help answer the open questions.

The foundation of this simulation is based on the work by Verma et al. [35], who, in turn, based their simulation on work by Zhang et al. [40]. It consists of a droplet modelled using an SPH model combined with a target modelled using a FEM model. The droplet and target interaction is modelled using a contact algorithm. The primary characteristics of the model and the deviations from the prior research will be discussed in the subsequent sections. Appendix A contains a complete list of the SPH keywords. Figure 3.7 shows a figure of the complete setup.

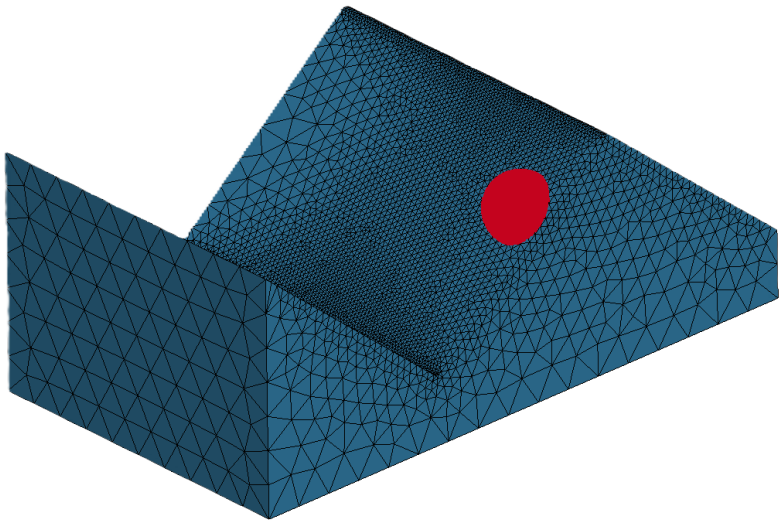

Figure 3.7: Overview of a droplet impact simulation setup for a 5mm, 40°, 0x sample. Consisting of 42.522 2nd order tetrahedral elements and 56552 SPH elements

3.5.1. SPH droplet

The droplet is modelled using the SPH generation tool in LS-PrePost, where a diameter and the number of SPH particles in the X, Y, and Z principle directions are required for a sphere. For these models, a diameter of 2mm and the number of particles specified are 60x60x60, resulting in a total of 113104 particles for a full sphere. However, due to a symmetry constraint, this is halved to 56552 SPH nodes.

The water droplet is described using an the *MATT NULL(009) material model combined with an equation of state (EOS) based on the Gruneisen formulation: *EOS GRUNEISEN, this equation of state characterises the compressibility relationship of the water thereby linking the volume, temperature and pressure of the water together. This is essential for calculating the mechanics during shock impacts. The exact values used are in section A.2. These values come from the research of Verma et al. [35].

3.5.2. FEM

The sample is modelled using a FEM model. For this study, the sample is modelled as an epoxy solid without any coating. This is chosen because obtaining a valid model for the coating used in the experiments would be a complex study. Due to the absence of a coating layer, mechanisms such as Rayleigh waves and the energy absorbance occurring do not accurately represent the real world. However, this simplified model is justified as the goal is not to predict the incubation time by using a complex model. Instead, it is used to gain insight into the differences in droplet impact for varying geometries. Here the geometries are more important than the material behaviour. In addition, since the epoxy is modelled as a simple linear plastic material instead of the visco-elastic material that it, in reality, is. This results in a lower amount of energy absorption and, thus, inaccurate modelling of material failure. This simple model was again chosen as obtaining accurate data on the epoxy used is difficult, and since the goal is not to predict the material failure, this effort is not justified. The keyword of the material model can be found in Figure A.3 in Appendix A.2.

The mesh consists of 2nd-order tetrahedral elements (*ELFORM 16 in LS-DYNA), which can better follow the surface contours than hexahedral elements. The elements are 2nd order as this allows a closer representation of the geometry and improves the simulation's accuracy. The meshes are created using the open-source program GMSH. As shown in Figure 3.7, the mesh is more refined towards the locations of impact and at the radii of the sample. An element size of roughly 0.25mm is used at the impact location, while a peak and valley radius of 0.2mm is split into elements covering 30 degrees. This mesh size was still too coarse to retrieve stress data accurately. However, the simulations were limited by the conditions of the LS-DYNA student license of a max of 128.000 nodes/elements.

3.5.3. Boundary conditions and contact

The boundary conditions imposed are the following, again, the specific keywords can be found in Appendix A.3 and A.4.

- Fixed boundary condition on the bottom notes to fix the sample in place. (BOUNDARY SPC SET)
- Symmetry conditions, to only model half of the problem, this is used so the element sizes could be further reduced while staying within the limits of the license. These conditions are:
  - Boundary symmetry plane (*BOUNDARY SPC SYMMETRY PLANE SET), constraining all nodes within a tolerance zone. It is located at the centre of the droplet impact location.
  - A symmetry plane for the SPH simulation (*BOUNDARY SPH SYMMETRY PLANE), located on the same plane as the FEM symmetry plane.
- Contact algorithm, this is identical to the one used in the research by Verma et al. [35], where it was found in the reference study to be in very close approximation to real-world experiments. Each cycle it checks if there is penetration between the SPH particles and the FEM elements. If there is penetration, a contact interface force is applied, which is equal to the product of the contact stiffness k and the penetration distance. A more thorough explanation can again be found in the work of Verma et al. [35].
- An initial velocity of -200 is applied to the SPH nodes (*INITIAL VELOCITY)

3.5.4. Test plan

The coupled simulations were performed to answer questions that arose from or were not yet answered by the experiments. Therefore, not all samples and impact locations were simulated. Instead, only samples and impact locations were simulated, and data was needed to answer open questions. The simulations are carried out as follows: First, the simulation was set up as described above. After running the simulations, the results are analysed using the post processing tool of LS-PrePost. Using this, the droplet behaviour and stress contours were plotted for various time steps. In addition to this, plot data for the vertical Force and Energy were outputted as .csv files so they could be properly plotted and analysed using Python scripts. Most of the time, the simulation was carried out for all three impact locations, as it is trivial to translate the droplet between the valley, mid and top, leading to little additional work to look at these locations. Table 3.3 provides an overview of all tested samples.

Angle [°]	Height [mm]	Spacing [-]	Simulated
0	0	0	x
20	5	0	
40	5	0	x
60	5	0	x
40	2	0	x
40	10	0	x
40	5	0.5x	x
40	5	1x	

Table 3.3: Overview of all simulated samples, each sample is simulated for the valley, mid and top.

3.5.5. Model limitations

A model always has limitations compared to the real world, the main limitations of this model are listed below:

- The research from Verma et al.[35] used a spherical droplet. Thus, this is what is verified in the simulations, and it is unknown what the accuracy of other droplet geometries would be. Therefore, in the simulations of this work also a spherical droplet is used, even though the droplets in the experiments are not actually spherical but instead are longitudinal jets.
- Due to the absence of a coating layer, phenomena that mostly occur within the coating layer in the real world are likely not accurately modelled. An example of this is stress waves, both travelling along the surface as well as reflecting multiple times within the coating.

- Due to the limitations on the maximum number of nodes/elements of the LS-DYNA student license, the mesh and droplet are relatively course and don't have the same level of fineness as was found to be optimal in the convergence study performed in the work of Verma et al. [35]. This leads to stress concentrations at impact likely being underestimated.
- It was noticed when looking at the energy plots, that the total energy in the system was significantly decreasing during the simulation, as is shown in Figure 3.8. At t=0, all energy is within the kinetic energy of the droplet, during impact, a portion of this energy is transferred to internal energy in the sample and to the contact algorithm which performs work on the droplet. In addition, a significant amount of energy disappears from the kinetic energy in the droplet but does not show up anywhere else. Thus, the energy has left the system, which is physically impossible.

  However, this is common in SPH modelling as it is a statistical model, and no conservation of energy rule is defined in the model. A steady, non-sudden delay of energy is acceptable. However, here, the loss in energy is about 20% of the system energy, which is considered as significant. This is probably comparable to the issue identified by Harazim [17] in his thesis. In cooperation with the LS-DYNA developers, he discovered that this energy loss in high-speed SPH contact is a bug. However, it was also found that this likely only significantly affects the energy balance and not the rest of the system.

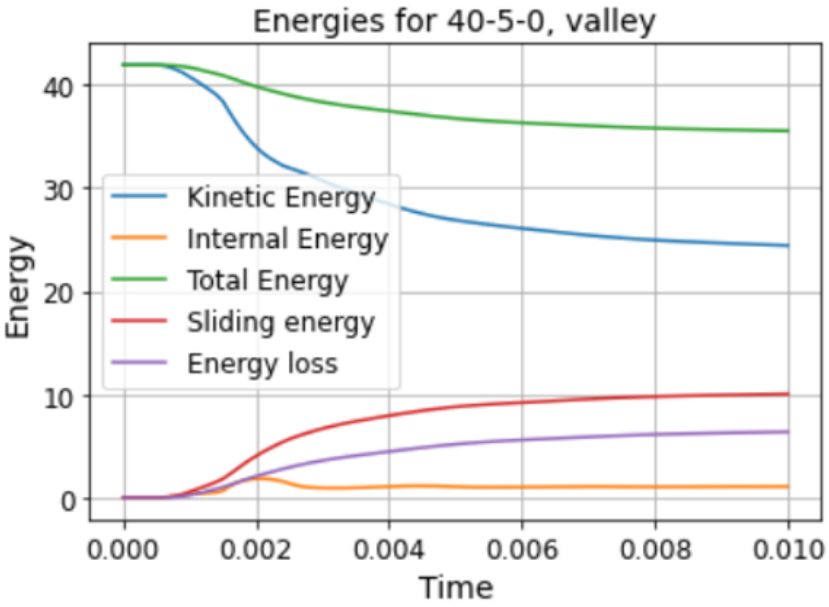

Figure 3.8: Energy balance of a droplet impact, showing the significant energy loss within the system.

4

Results and discussion

This chapter will present the results obtained from the experimental and numerical studies. This will be done by presenting and discussing the results separately for each sub-question. Each sub-question starts with a general overview of the experiment and presents the experimental findings. Next, the experimental data will be interpreted using literature and data from the numerical study.

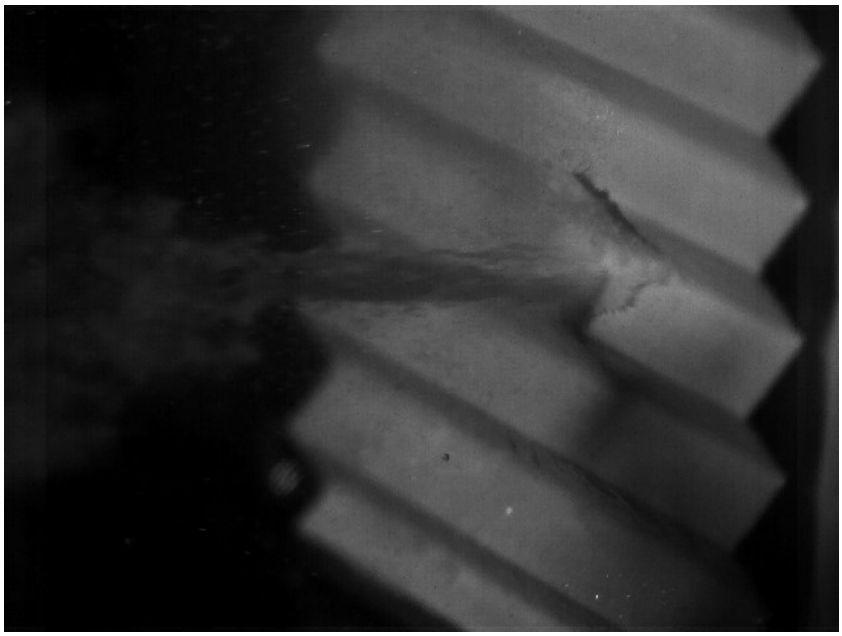

Figure 4.1: High speed footage of the PJET hitting a [40°, h=5mm, s=0x] sample in the mid.

To better understand what both a droplet impact and the resulting damage after experiments look like. First, some examples of both will be provided and explained. In Figure 4.1, one can see the impact of a PJET droplet on the surface. It is clearly visible that the droplet is indeed not a sphere but a longitudinal jet.

The results of the tests on this [40°, h=5mm, s=0] sample are shown in Figure 4.3. As one can see, there is quite a significant spread. This was observed in all experiments and is also in line with findings from Alonso Diaz [1].

The incubation times and the dimensions of the damaged locations were studied. Figure 4.8 shows an example of this. This is a top-down view of the damage, which means there is a parallax error due to the slanted shape of the surface. However, since this is the same plane as how the droplet travels, this is deemed preferable over corrected versions, which will produce artefacts due to inconsistencies in the top and bottom.

Additionally, the cross-sections of the samples were analysed under the microscope to examine the layer thickness. This was done by casting them in epoxy and then sanding and polishing the epoxy slug to a smooth surface. They could then be viewed under the microscope. The results from this are shown in tables by their corresponding sub-questions.

4.1. Impact location

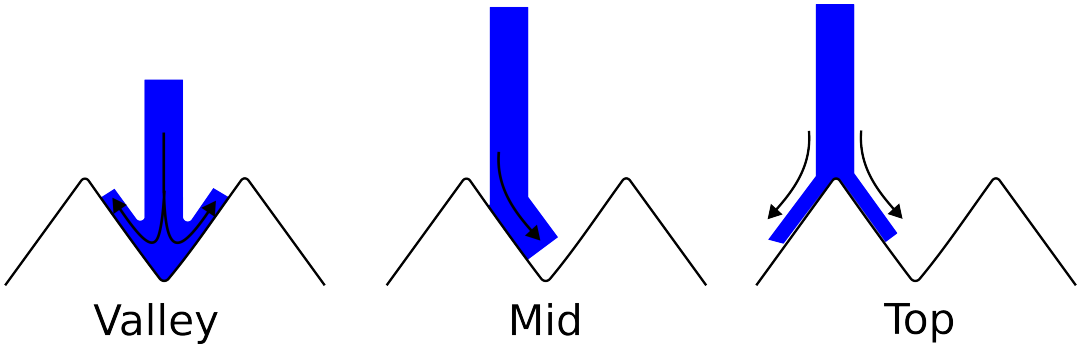

Figure 4.2: Schematic representation of droplet impact for different impact locations

The first sub-question will be discussed: How is the erosion resistance affected by the impact location? To answer this the samples have been tested at different impact locations, the top, middle and valley, as is schematically shown in Figure 4.2. Before the experiments, it was hypothesised that the valley would have a lower incubation time than the mid and top as there was nowhere for the water to go, thus increasing pressures and leading to a shorter incubation time. In addition, the top was also expected to have a lower incubation time as this is a very thin section and, as such, is more likely to get damaged due to a stress concentration.

The results of the experiments are shown in Figure 4.3, with the exact values of the median shown in Table 4.1. As one can see, the mid has a higher incubation time than the top and valley, which aligns with the hypothesis. To better understand these results, one can look at the simulated impact for the valley, mid and top in Figures 4.4, 4.5 and 4.6 respectively. These three figures show both a plot of the SPH particles hitting the sample and contour plots of the von Mises stress on the sample's surface.

As one can see in the valley impact in Figure 4.4, the droplet first impacts at the two sides, after which the impacting water is directed into the valley, where it then collides together with the rest of the droplet, resulting in a high force and stress concentration. This high force compared to the mid and top impact can also be seen in Figure 4.7, where the vertical force acting on the sample is shown for all three impact locations. This high force and resulting stress is a good explanation for the lower incubation time in the valley. However, when considering the variations in stress alongside insights from the Springer model, which links stress to incubation time through Equation 4.1 it becomes evident that the discrepancy in stress levels would lead to a more significant reduction in incubation time than the observed 60% decrease. Equation 4.1 shows the relationship between stress and incubation time, derived from the Springer model in Equation 2.6.

$$n_i \propto \left(\frac{1}{P}\right)^{5.7} \tag{4.1}$$

This variation can be attributed to the differences in coating layer thickness observed between the valley and the midpoint, as outlined in Table 4.1.

A second point that refers to the difference in layer thickness between the mid and valley is shown in Figure 4.5. At T=0.015ms, the stresses of the water reaching the valley are higher compared to the mid location. An explanation for this could again be the difference in layer thickness between the mid and the valley. An additional explanation would be that the mesh sizes in the simulations are too coarse to obtain the peak impact stresses properly, leading to the above comparison not being accurate.

Another observation from Figure 4.3 shows that the top has the lowest incubation time. However, this would not be expected when looking at the stress and force plots from the simulations. Here, the stresses and forces are slightly higher than the mid but significantly lower than the valley. This

discrepancy between the simulation and the experiments can again be attributed to the substantially lower layer thickness at the top.

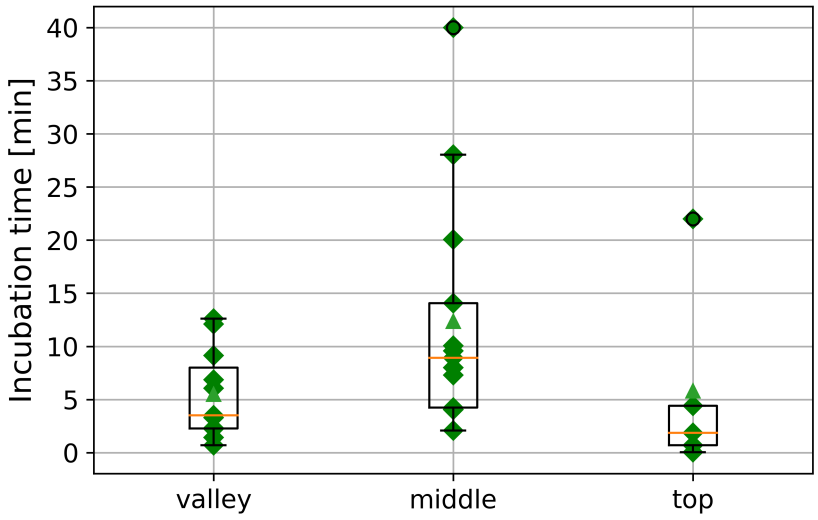

Figure 4.3: Incubation time of the [a=40°, h=5, s=0] sample for varying impact locations

Location	Median Incubation time [min]	Coating layer thickness [um]
Valley	3.5	472
Mid	8.9	286
Top	1.9	100

Table 4.1: Median incubation time and coating thickness of the [40°, h=5mm, s=0] sample for varying impact locations

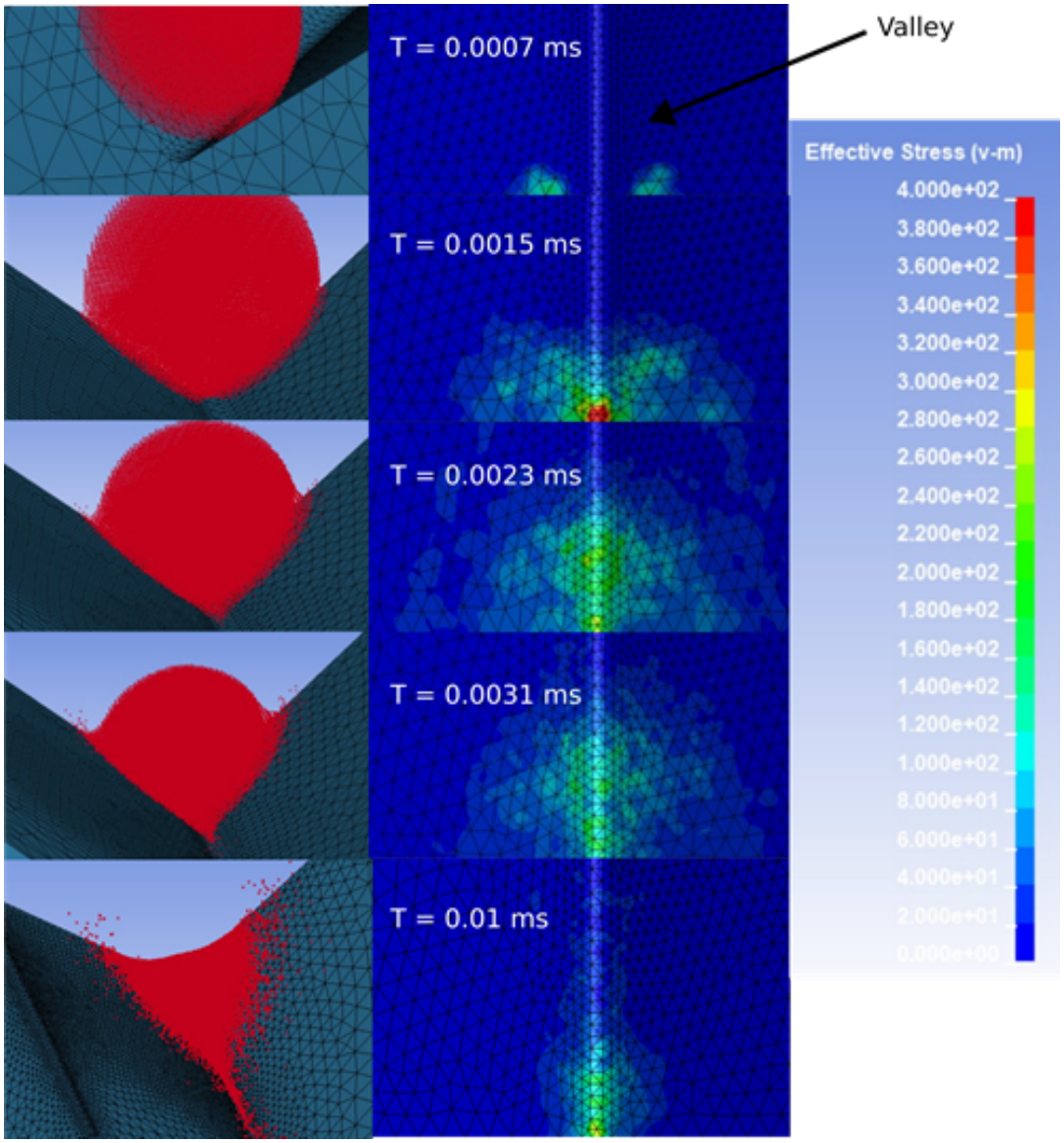

Figure 4.4: Overview and Von Mises stress contour plot of valley impact. Note: scale 0-400[MPa]

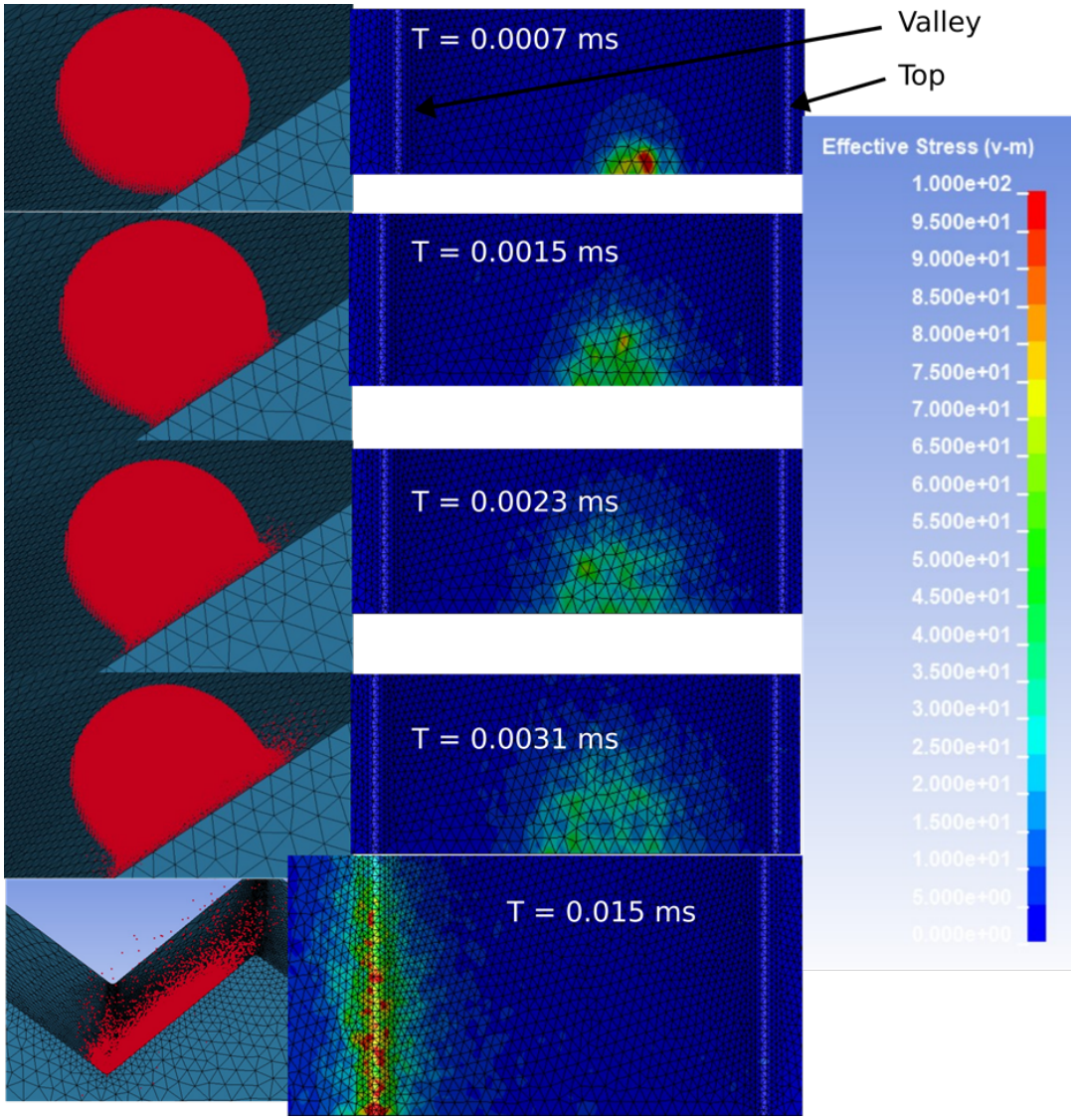

Figure 4.5: Overview and Von Mises stress contour plot of mid impact. Note: scale 0-100[MPa]

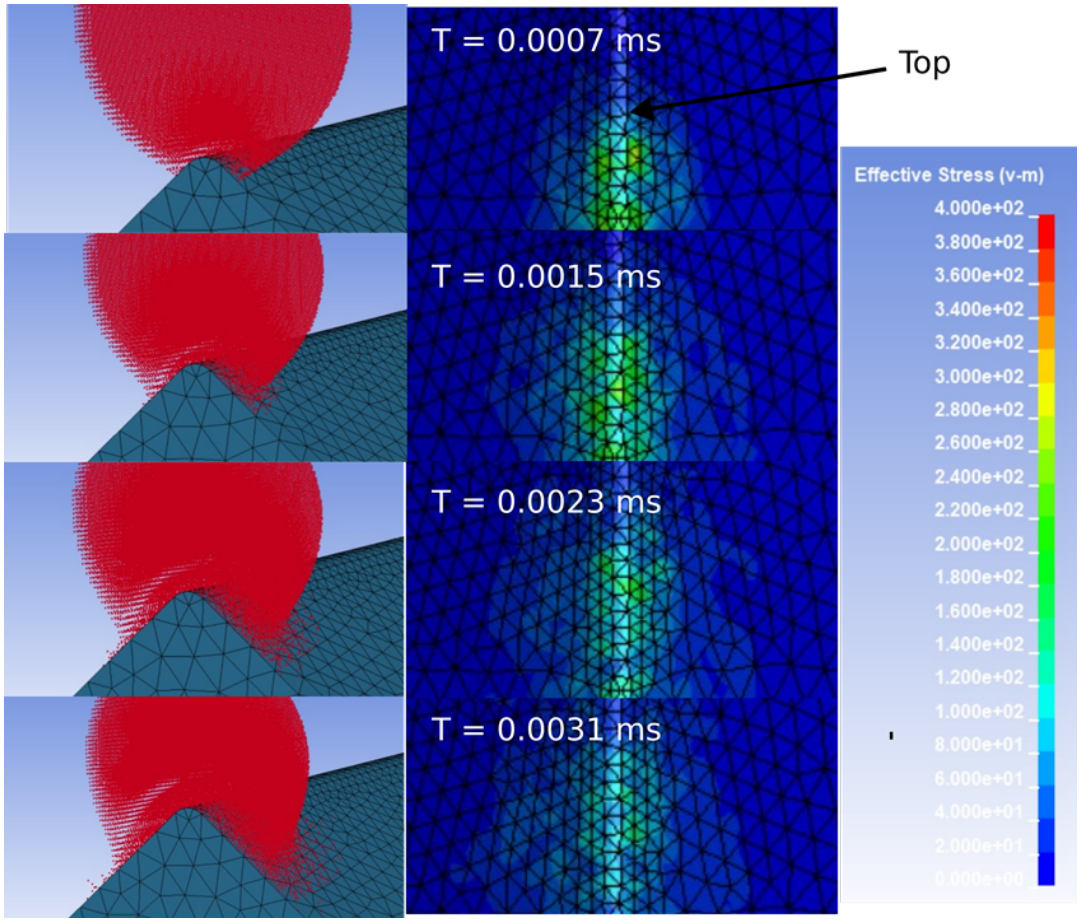

Figure 4.6: Overview and Von Mises stress contour plot of top impact. Note: scale 0-400[MPa]

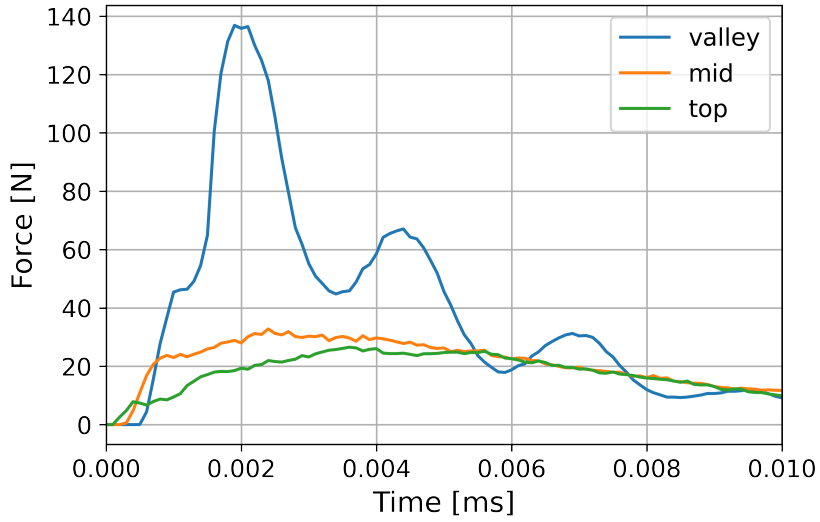

Figure 4.7: Vertical force of droplet for [a=40°, h=5, s=0] sample

In addition to the incubation time, the actual damage was also studied. It was observed that the damage was not equal everywhere. For each impact, the dimensions of the damaged area were observed using the microscope. An example is shown in Figure 4.8. As one can see, the valley's damage is roughly equal in size in X and Y, or ΔY is larger than ΔX. However, especially for the mid

but also for the top, ΔX is significantly larger than ΔY. This can likely be explained by the damage due to lateral jetting after incubation. For the valley, the lateral jetting is mainly in the Y direction since, in the X direction, there is nowhere to go, while for the mid and top, the droplet travels downwards along the slanted surface, being in the X direction. The circular damage of the valley can be explained by the lateral jetting being in the Y direction while the projection due to the slanted surface works in the X direction.

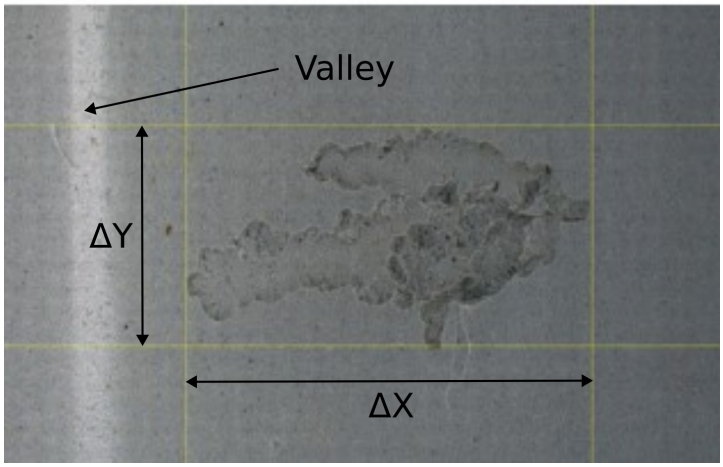

Figure 4.8: Top down view of Delta X and Y dimensions for an impact location.

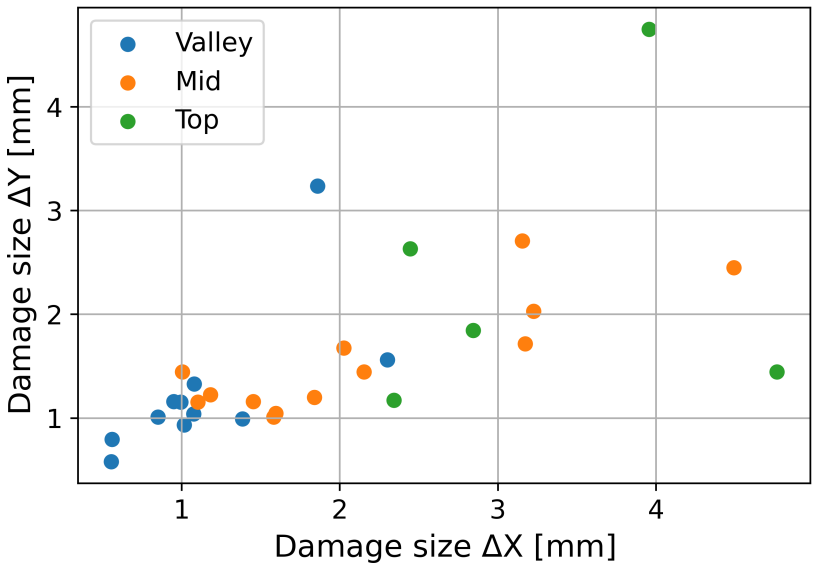

Figure 4.9: Scatter plot of the damage dimensions of the [40°, h=5mm, s=0] sample for varying impact locations

4.2. Feature angle

The second sub-question studied is: How does the angle of the slanted surfaces affect the erosion resistance? To answer this question, three samples with angles of 20°, 40° and 60°, as shown in Figure 4.10, have been tested. It was hypothesised that based on the Springer model and numerical studies, there would be a substantial difference in incubation time between the samples, where the 60° sample would have the highest incubation time and the 20° sample would have the lowest incubation time. This is because the more angled surface experiences much lower impact stresses from the droplet compared to the less slanted surface. This is also shown in Equation4.2, where the theoretical performance of an angled plate relative to a flat plate is shown based on the Springer model. When

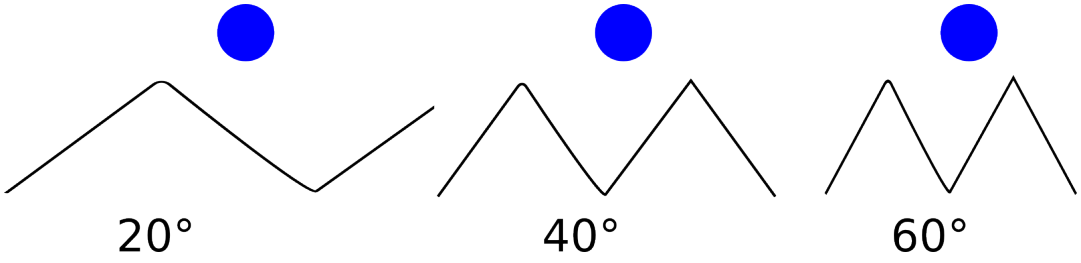

Figure 4.10: Schematic representation of droplet impact for different feature angles

looking at the experimental results in Figure 4.11 and Table 4.2, this hypothesis holds for the 20° and 40° samples. When one looks at the predicted values from the Springer model based on the performance of the flat plate in Table 4.3, the actual performance at the mid is very close to the predictions. However, the 60° sample performs equal in the mid to the 40° sample. The equation used to calculate the expected performance based on the Springer model is shown in Equation 4.2

$$n^i_{a,predicted} = \frac{n^i_{flat}}{cos(a)^{5.7}} \tag{4.2}$$

Here, $n^i_{a,predicted}$ is the predicted incubation time based on the incubation time of the flat plate n^i_{flat} and feature angle a.

A partial explanation for this can again be found when looking at the layer thickness in Table 4.4, where one can see that the layer thickness in the mid is significantly thinner for the 60° sample compared to the other two samples. An additional reason can be found in the impact location of the droplet. This impact location is shown in Figure 4.12, showing that the droplet aimed at the mid actually impacts close to the top. The stress contour plot in Figure 4.13 shows that due to the droplet impacting close to the top, a significant amount of stress is present at the top. Combined with the thinnest layer thickness near the top, this can explain the premature failure of the 60° sample.

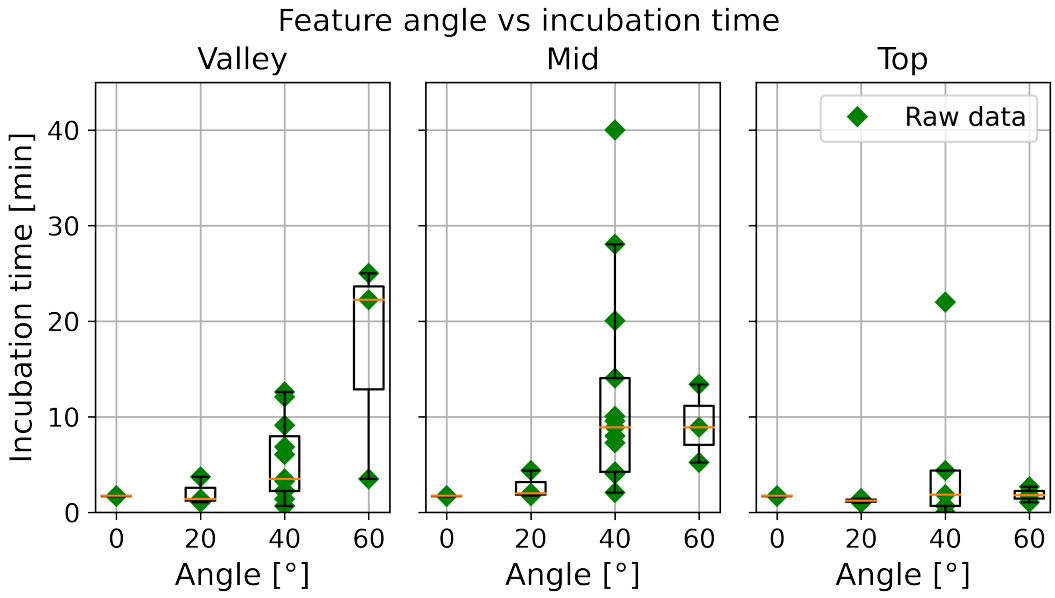

Figure 4.11: Plots of incubation time as a function of feature angle for different locations.

Angle [°]	Valley [min]	Mid [min]	Top [min]
0	1.8	1.8	1.8
20	1.4	2.0	1.2
40	3.5	8.9	1.9
60	22.3	8.9	1.8

Table 4.2: Median incubation time for the different impact angles

Angle [°]	Predicted [min]	measured [min]
flat	-	1.8
20	2.5	2.0
40	8.0	9.0
60	90.0	8.9

Table 4.3: Incubation time at the mid location for different angles as predicted by the Springer model compared to the measured values

Angle[°]	Valley [um]	Mid [um]	Top [um]
20	328	220	150
40	472	286	100
60	311	150	128

Table 4.4: Layer thickness for the different angled samples and different locations

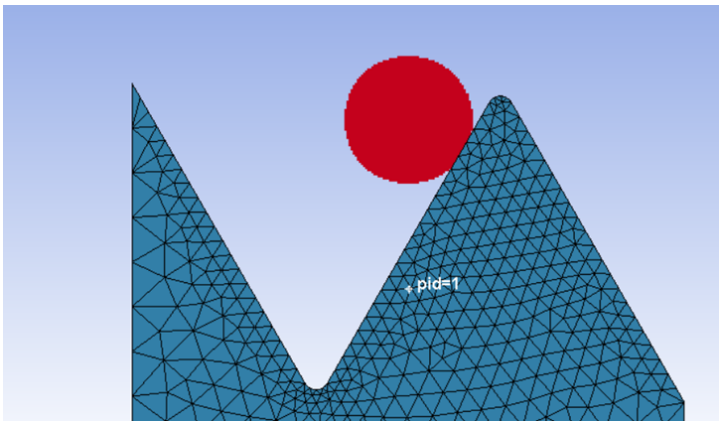

Figure 4.12: Impact location for the [60°, h=5mm, s=0] sample showing that droplet aimed at the mid impacts close to the top.

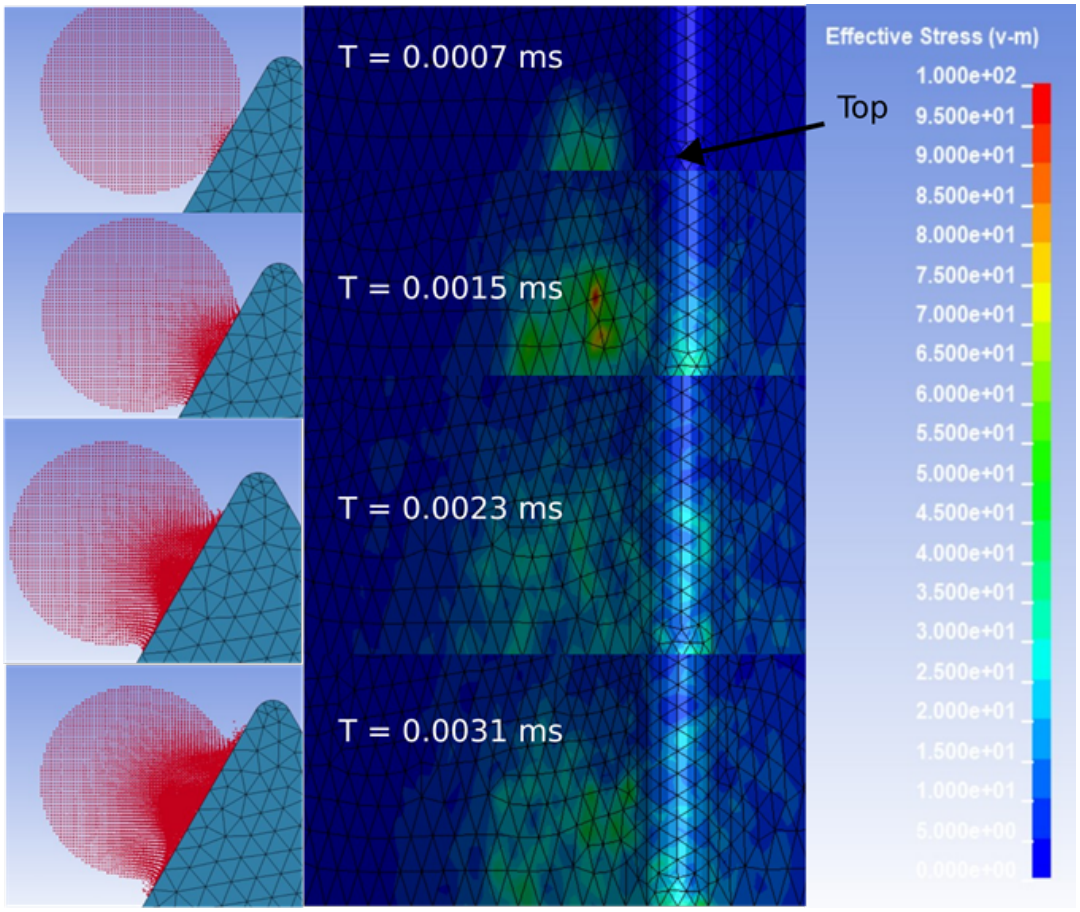

Figure 4.13: Overview and Von Mises stress contour plot of mid impact for the [60°, h=5mm, s=0] sample. Note: scale 0-100[MPa]

In addition to the lower-than-expected incubation times for the 60° sample, it was also noticed that the damage would always occur at the top, even when the droplet was aimed at the valley. When looking at the results from the simulations, a possible explanation can be found in the stress wave travelling from the valley, as is shown in Figure 4.14. As one can see the stress wave on the 60° sample has a higher magnitude than the wave on the 40° sample. However, it is not clear how accurate these stress waves are. This is because it is possible that the stress wave behaves very differently when a coating is present and possibly very dependent on the mesh size.

A contributing factor is the peak stress in the valley for both impacts. As shown in Figure 4.15, the peak stress for the 60° sample is significantly lower than the 40° sample. It is possible that this leads to a delay in damage occurring in the valley, leading to damage occurring at the top due to the stress wave. However, this is only a hypothesis and needs further study in future work.

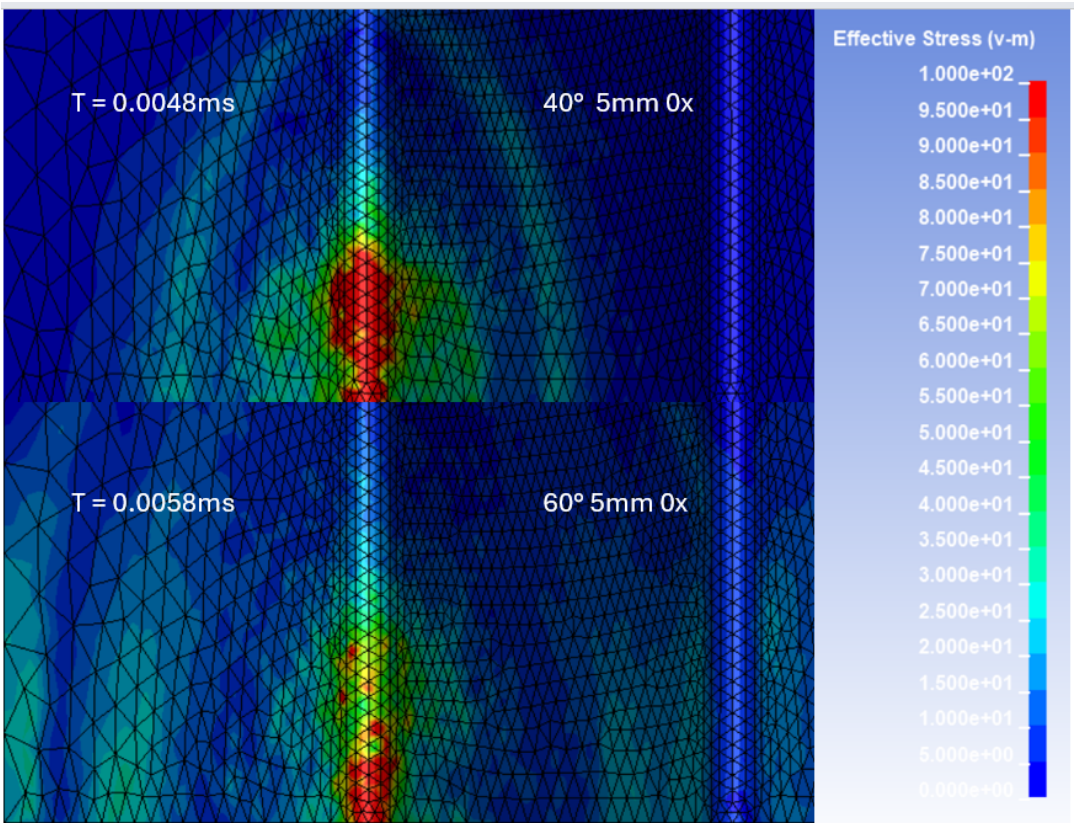

Figure 4.14: Stress wave traveling from the 40° and 60° sample upwards towards the top. Note: scale is 0-100 MPa

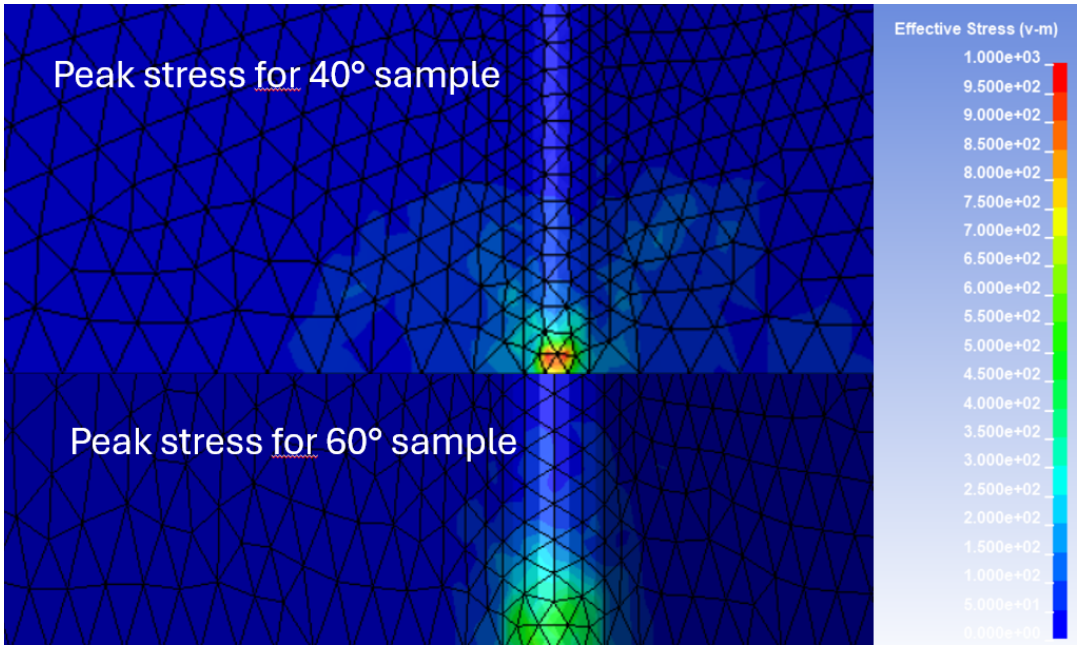

Figure 4.15: Peak stress in the valley impact for the 40° and 60° sample. Note scale is 0-1000MPa

4.3. Feature height

The third sub-question studied is: How does the height of the slanted surfaces affect the erosion resistance? Three 40° samples with a height of 2, 5 and 10mm were produced, schematically shown in

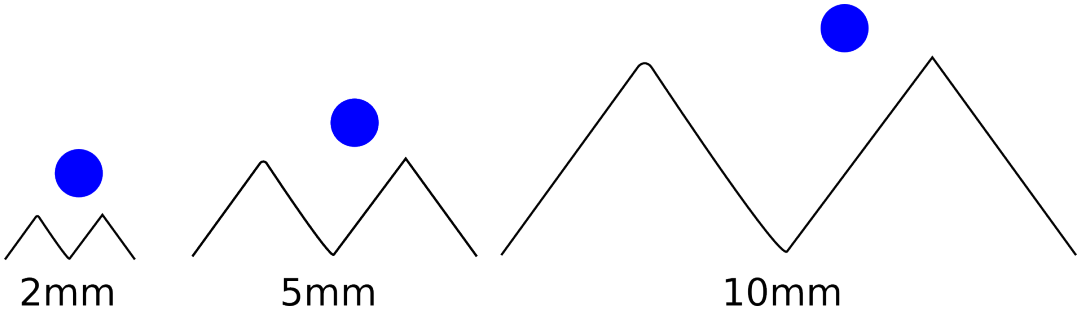

Figure 4.16: Schematic representation of droplet impact for different feature heights

Figure 4.16. It was hypothesised that when making the feature size smaller, at some point, there would be a significant deviation from an angled plate due to influences from the top and valleys present.

Looking at the results in Figure 4.17 and the median values in Table 4.5, one can see that for the mid, the 2mm sample seems to have a lower incubation time compared to the 5 and 10mm sample. This can be explained by looking at the force plots in Figure 4.18. For the 2mm sample, after the initial impact, the force increases further, while for the other two samples, the force decreases. This increase in force is due to the droplet reaching the valley of the sample while the droplet is still tightly together and still has most of its momentum. In addition, the droplet initial is also close to the top, similar to the previous 60° sample. This again results in a stress concentration near the top combined with the lower layer thickness resulting in a shorter incubation time. Also for this sample, most of the damage was observed near the top, even for the valley thickness. A similar explanation as with the 60° sample is also expected to play a role here.

One can see in Figure 4.17 that the 10mm sample's incubation time seems higher compared to the other samples. However, the large variance in incubation time can also easily be attributed to statistical error. A possible reason for this is the vertical force plot in Figure 4.18. As one can see the 5 and 10mm sample start out identical, however after 0.01ms the droplet of the 5mm sample starts to reach the valley, and the vertical force increases. For the 10mm sample, this is not the case, and the valley is only reached after 0.02 ms, at which point much of the momentum has already dissipated, and the droplet has spread out, resulting in a significantly lower force. However, if these droplets hitting the valley would contribute to the incubation time, it would be expected that the damage would then be in the valley. This is, however, not the case.

A second explanation could be the aforementioned stress waves. However, for both of these samples, the magnitude of the stress waves is small, making it unlikely that these have much of an effect. Aside from these points, no other indicators have been found to attribute the difference in the 5 and 10mm samples. Thus, it can be concluded that the difference in the 5 and 10mm samples is likely due to statistical variance and that there is no real difference between the performance of the 5 and 10mm samples.

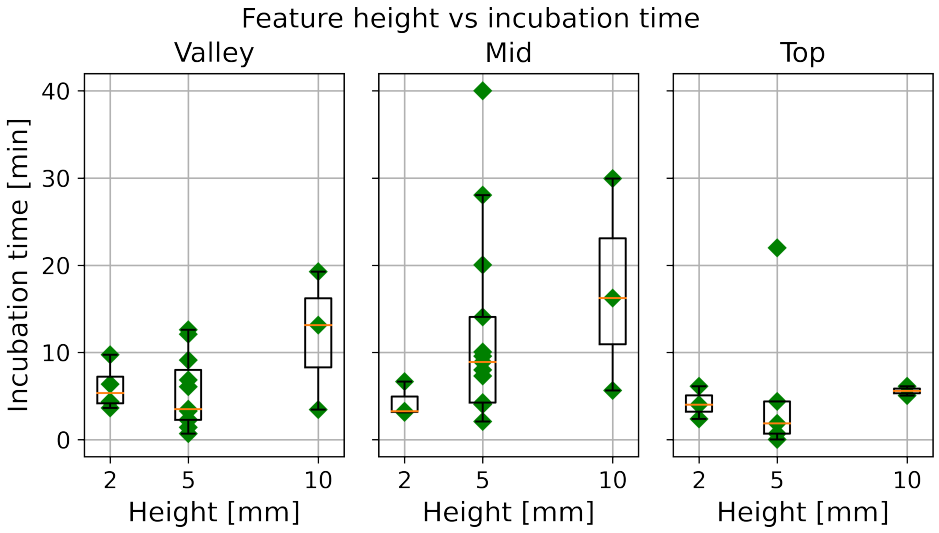

Figure 4.17: Plots of incubation time as a function of feature height for different locations.

height [mm]	Valley [min]	Mid [min]	Top [min]
0	1.8	1.8	1.8
2	5.4	3.3	4.0
5	3.5	8.9	1.9
10	13.2	17.3	5.6

Table 4.5: Median incubation time for the different feature heights

Height	Valley [um]	Mid [um]	Top [um]
2mm	366	288	150
5mm	472	286	100
10mm	380	266	200

Table 4.6: Layer thickness for the samples with different heights and different locations

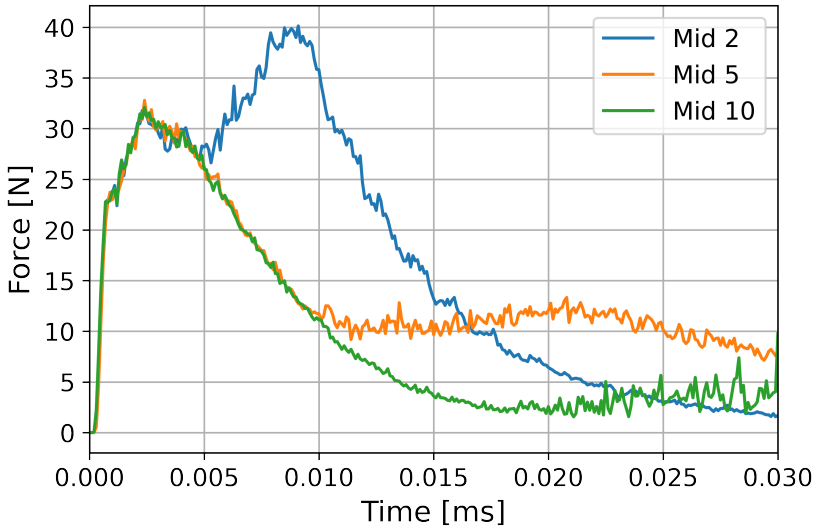

Figure 4.18: Vertical reaction force on droplet impact of samples of varying height

4.4. Feature spacing

The final sub-question studied is: How does the spacing between the slanted surfaces affect the erosion resistance? It was hypothesised that spacing out the locations where the surfaces meet, i.e. increasing the feature spacing, would affect the incubation time. Three samples with 0, 0.5x and 1x spacing were tested to test this, as shown schematically in Figure 4.19. These spacings were derived from the spacings often observed in nature. The results from these experiments are shown in Figure 4.20. As one can see, the valley and top for both spaced samples perform equally to a flat plate. This indicates that the transition region from top or valley behaviour to flat plat behaviour must lie somewhere between 0 and 0.5x spacing, investigating this region would be interesting for future work.

A second observation is that the median values of the spaced sample are higher compared to the non-spaced sample. It is concluded that this is most likely due to variance in the results. Below are the reasons listed that lead to this conclusion:

- When looking at the layer thickness for mids in the different samples in Table 4.8, no significant differences are observed. Thus, this is not the cause of the difference in incubation time.
- In the simulations, no differences were observed for either the impact force or energy dissipation. Therefore, this is also not the reason for the observed difference.
- A possible explanation is the absence of a valley, leading to less stress near the valley for the spaced samples. However, this is counteracted by the lower layer thickness in the valleys for the spaced samples, likely negating these results.

Since none of these points provides a convincing explanation for the difference in performance, it may be due to the variance in the experimental results.

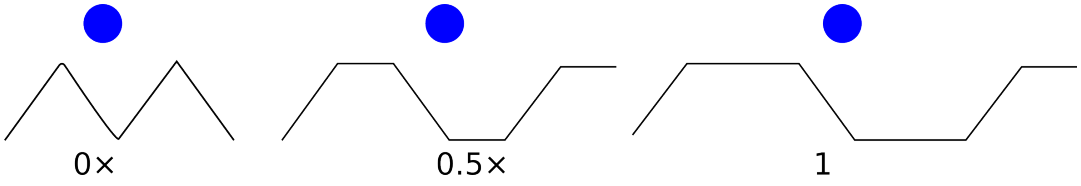

Figure 4.19: Schematic representation of droplet impact for different feature spacing

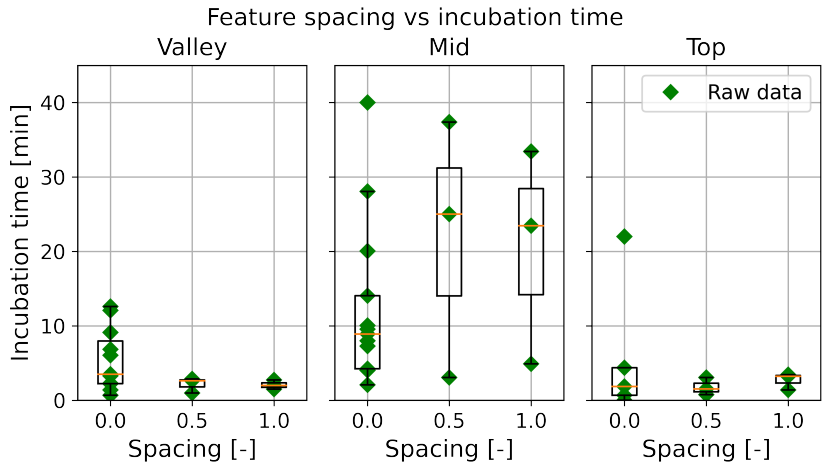

Figure 4.20: Plots of incubation time as a function of feature spacing for different locations.

spacing [mm]	Valley [min]	Mid [min]	Top [min]
flat	1.8	1.8	1.8
0x	3.5	8.9	1.9
0.5x	2.6	25.0	1.5
1x	2.0	23.5	3.3

Table 4.7: Median incubation time for the different feature spacings

Spacing	Valley [um]	Mid [um]	Top [um]
0x	472	286	100
0.5x	270	245	260
1x	297	190	204

Table 4.8: Layer thickness for the samples with different spacing and different locations

5

Conclusions and recommendations

This thesis studied if the erosion resistance of wind turbine blades could be improved by adding features to a flat sample inspired by erosion-resistant organisms. To do this, experimental and numerical studies were carried out to study the effect of impact location and triangular features' angle, height and spacing. This was done using the PJET experimental method and the coupled FEM-SPH numerical method. After analysing the results, the four sub-questions, and in turn the main question can be answered, which will be done below:

How is the erosion resistance affected by the impact location?
After studying the results belonging to these sub-questions, several key points can be concluded:

- Impact stresses and forces are significantly higher for valley impacts. While this study looked specifically into valley impacts, it is likely that this can be generalised to liquid droplet impacts onto concave surfaces, where the radius of the concave surface is smaller than the droplet's radius. This results in the droplet first hitting the multiple side locations, forcing the water into the centre of the concave surface, leading to a very high-pressure point.
- Forces and stresses are relatively comparable between the mid and top impact locations. Differences in incubation time between those locations in this study can be attributed to the significant difference in layer thickness.
- It was found that damage shapes are not always circular for angled impact. It is likely that the damage shape after incubation follows the direction of lateral jetting. Likely this holds more universally, also outside this study, although no other examples have been found.

How does the angle of the slanted surfaces affect the erosion resistance?

- As was expected from the theory, the impact angle significantly affected incubation time, following the predictions from the Springer model. Deviations from this can again be explained by the variations in layer thickness.
- It was found that the damage would always occur near the top for the [60°, h=5mm,s=0x] and [40°, h=2mm, s=0x] samples. Reasons for this were explored, however no satisfactory explanation has been found.

How does the height of the slanted surfaces affect the erosion resistance?

- It was found that the 5 and 10mm samples performed similarly, while the 2mm sample performed significantly worse. For the small features, the impact will always be close to a top or valley where the incubation time is lower. Thus, it can be concluded that once the features become close to the size of the droplet, performance starts to deviate from that of the larger samples.

How does the spacing between the slanted surfaces affect the erosion resistance?

- The spacings used in this study, 0.5x and 1x, resulted in top and valley behaviour identical to that of a flat plate. The mids performed identically to the non-spaced sample. It is likely that between the non-spaced sample and the 0.5x spacing lies a transition region where the high forces decrease, leading to a possible longer incubation time if the layer thickness is equal.

Answering these four sub-questions leads to the following answer on the main research question:
How does the integration of slanted surfaces to the surface morphology, inspired by erosion-resistant organisms, impact the resistance to leading edge erosion in wind turbine blades?

It can be concluded that the erosion resistance of a surface can indeed be improved by adding slanted surfaces, similar to those seen in erosion-resistant organisms. It has been found that the impact angle has a very significant effect on the erosion resistance. In addition, performance varies based on the impact location, particularly when the valley sees high stresses. Care should thus be taken around the valley when designing a geometry. It has been found that the size of the features is not critical, however when the size of the impacting droplets comes close to the size of the features, edge effects become more pronounced and thus performance suffers.

5.1. Recommendations

While this study gathered a lot of new knowledge, it also raised new questions. Looking back, there are things that would have improved the quality of the study if they had been done differently. First, these improvement points will be listed below. Next, some options for future work will be suggested. The things that would have improved the study if they were done differently are:

- Having a constant layer thickness. A lot of the differences observed are now most likely explained by layer thickness. However, if the layer thickness had been equal for all samples, the quality of the experiments would have vastly improved. Two suggestions to realise this would be: (1) Making the layer thickness equal by using a moulding process, similar to over-moulding an injection mould. While this is not a recommended process by the coating manufacturer, it could be tested if the performance of a coating layer applied this way is equal to that of a sprayed coating. (2) Continue spraying the coating, however now make it thick enough so that the layer thickness no longer has a large influence, as was seen in the study from Hoksbergen et al.[19], after a certain thickness the material behaves like a bulk material and further changes in thickness no longer have a significant effect.
- Use smaller spacings, between 0x and 0.5x, to better understand the droplet behaviour in the valley.

Interesting questions that were raised during this study and points that are interesting but were not included due to the need for a limited scope in this study are:

- Why is there no damage visible in the valleys for the [60°, h=5mm, s=0] and [40°, h=2mm, s=0] samples? What are the conditions for this behaviour to occur? A suggestion to further study this would be to use constant layer thickness and separately study the height, width and angle of these smaller samples to better understand what is happening.
- Not only use spacing between features, but also use different geometry such as large radii, for the valley for example it would be interesting to see how the behaviour would change is the radius of the valley is larger compared to the radius of the droplet.
- In nature, the geometries are often more complex than simple ridges. For example, domes are an often-seen feature of organisms. It would be interesting to study how these 3d features would compare to the 2d features (triangles) used in this study.

References

[1] Miguel Alonso Díaz. *Leading Edge Erosion Effect of droplet impact frequencies and dry intervals on incubation times of polyurethane coatings*. 2021.

[2] B. Amirzadeh et al. “A computational framework for the analysis of rain-induced erosion in wind turbine blades, part I: Stochastic rain texture model and drop impact simulations”. In: *Journal of Wind Engineering and Industrial Aerodynamics* 163 (Apr. 2017), pp. 33–43. ISSN: 01676105. DOI: 10.1016/j.jweia.2016.12.006.

[3] Mohammed M. Atif et al. “Evaluation of breaking wave effects in liquid sloshing problems: AN-CF/SPH comparative study”. In: *Nonlinear Dynamics* 97.1 (July 2019), pp. 45–62. ISSN: 1573269X. DOI: 10.1007/s11071-019-04927-5.

[4] A. C. Best. “The size distribution of raindrops”. In: *Quarterly Journal of the Royal Meteorological Society* 76.327 (1950), pp. 16–36. ISSN: 1477870X. DOI: 10.1002/qj.49707632704.

[5] J H Brunton. “A. THE PHYSICS OF IMPACT AND DEFORMATION: SINGLE IMPACT I. High speed liquid impact”. In: *ilosophical Transactions of the Royal Society of London. Series A, Mathematical and Physical Sciences* 260.1110 (1966), pp. 79–8. URL: https://royalsocietypublishing.org/.

[6] Charles B. Burson-Thomas et al. “Importance of Surface Curvature in Modeling Droplet Impingement on Fan Blades”. In: *Journal of Engineering for Gas Turbines and Power* 141.3 (Mar. 2019). ISSN: 15288919. DOI: 10.1115/1.4041149.

[7] Zheng Cao et al. *Formation mechanism and detection and evaluation methods as well as repair technology of crack damage in fiber-reinforced composite wind turbine blade: a review*. June 2022. DOI: 10.1007/s00170-022-09230-z.

[8] Junlei Chen, Jihui Wang, and Aiqing Ni. *A review on rain erosion protection of wind turbine blades*. Jan. 2019. DOI: 10.1007/s11998-018-0134-8.

[9] DUCOM. *Operation & Testing Manual of Liquid Droplet Erosion Tester*. 2020.

[10] Energy technology centre. *Blade leading edge erosion*.

[11] N. Fujisawa and A. Aihara. “Rain erosion mechanism on a leading-edge half cylinder”. In: *Wear* 532-533 (Nov. 2023). ISSN: 00431648. DOI: 10.1016/j.wear.2023.205103.

[12] Ross Gunn and Gilbert d. Kinzer. “The terminal velocity of fall for water droplets in stagnant air.” In: *Journal of atmospheric sciences* 6.4 (1949), pp. 243–248.

[13] Zhiwu Han et al. “An Efficient Bionic Anti-Erosion Functional Surface Inspired by Desert Scorpion Carapace”. In: *Tribology Transactions* 58.2 (Mar. 2015), pp. 357–364. ISSN: 1547397X. DOI: 10.1080/10402004.2014.971996.

[14] Zhiwu Han et al. “Anti-erosion function in animals and its biomimetic application”. In: *Journal of Bionic Engineering* 7.SUPPL. (Sept. 2010). ISSN: 16726529. DOI: 10.1016/S1672-6529(09)60217-1.

[15] Zhiwu Han et al. *Biomimetic multifunctional surfaces inspired from animals*. Aug. 2016. DOI: 10.1016/j.cis.2016.03.004.

[16] Zhiwu Han et al. “Erosion-resistant surfaces inspired by tamarisk”. In: *Journal of Bionic Engineering* 10.4 (Oct. 2013), pp. 479–487. ISSN: 16726529. DOI: 10.1016/S1672-6529(13)60238-3.

[17] Mateusz Harazim. *Hypervelocity Impact Simulation using Smoothed-Particle Hydrodynamics*. Tech. rep. 2023.

[18] F. J. Heymann. “High-speed impact between a liquid drop and a solid surface”. In: *Journal of Applied Physics* 40.13 (1969), pp. 5113–5122. ISSN: 00218979. DOI: 10.1063/1.1657361.

[19] Theodorus Hendrikus Hoksbergen, R. Akkerman, and I. Baran. “Fatigue lifetime prediction model for leading edge protection coating systems of wind turbine blades”. In: *Tribology International* 189 (Nov. 2023). ISSN: 0301679X. DOI: 10.1016/j.triboint.2023.108901.

[20] Theodorus Hendrikus Hoksbergen, Remko Akkerman, and Ismet Baran. “The Springer Model for Lifetime Prediction of Wind Turbine Blade Leading Edge Protection Systems: A Review and Sensitivity Study”. In: *Materials* 15.3 (Feb. 2022). ISSN: 19961944. DOI: 10.3390/ma15031170.

[21] He Huang, Yan Zhang, and Luquan Ren. “Particle Erosion Resistance of Bionic Samples Inspired from Skin Structure of Desert Lizard, Laudakin stoliczkana”. In: *Journal of Bionic Engineering* 9.4 (Dec. 2012), pp. 465–469. ISSN: 16726529. DOI: 10.1016/S1672-6529(11)60141-8.

[22] Mohamed Elhadi Ibrahim and Mamoun Medraj. *Water droplet erosion ofwind turbine blades: Mechanics, testing, modeling and future perspectives*. Jan. 2020. DOI: 10.3390/ma13010157.

[23] Sohyun Jung et al. “Anti-erosive mechanism of a grooved surface against impact of particle-laden flow”. In: *Wear* 406-407 (July 2018), pp. 166–172. ISSN: 00431648. DOI: 10.1016/j.wear.2018.04.008.

[24] M H Keegan, D H Nash, and M M Stack. “On erosion issues associated with the leading edge of wind turbine blades”. In: *Journal of Physics D: Applied Physics* 46.38 (2013), p. 383001.

[25] Michael Liebreich. *London summit 2017*. 2017.

[26] Agrim Sareen, Chinmay A Sapre, and Michael S Selig. *Effects of Leading-Edge Protection Tape on Wind Turbine Blade Performance*. Tech. rep. 5. 2012, pp. 525–534.

[27] Amrit Shankar Verma et al. “Effects of onshore and offshore environmental parameters on the leading edge erosion of wind turbine blades: A comparative study”. In: *Journal of Offshore Mechanics and Arctic Engineering* 143.4 (Aug. 2021). ISSN: 1528896X. DOI: 10.1115/1.4049248.

[28] George S. Springer. *Erosion by liquid impact*. Scripta Pub. Co., 1976. ISBN: 0470151080.

[29] S. Stanly and B.A. Cook. “Erosion by water-hammer”. In: *Proceedings of the Royal Society of London. Series A, Containing Papers of a Mathematical and Physical Character* 119.783 (1928), pp. 481–488. ISSN: 20539150.

[30] G.P. Thomas and J.H. Bruntont. “Drop impingement erosion of metals”. In: *Proc. Roy. Soc. Lond. A* 314 (1970), pp. 549–565. URL: https://royalsocietypublishing.org/.

[31] J. Tong et al. “Two-body abrasive wear of the outside shell surfaces of mollusc Lamprotula fibrosa Heude, Rapana venosa Valenciennes and Dosinia anus Philippi”. In: *Tribology Letters* 19.4 (Aug. 2005), pp. 331–338. ISSN: 10238883. DOI: 10.1007/s11249-005-7450-8.

[32] Jin Tong et al. “Abrasive wear of embossed surfaces with convex domes”. In: *Wear* 274-275 (Jan. 2012), pp. 196–202. ISSN: 00431648. DOI: 10.1016/j.wear.2011.08.027.

[33] Amrit S. Verma et al. “Leading edge erosion of wind turbine blades: Effects of blade surface curvature on rain droplet impingement kinematics”. In: *Journal of Physics: Conference Series*. Vol. 1618. 5. IOP Publishing Ltd, Sept. 2020. DOI: 10.1088/1742-6596/1618/5/052003.

[34] Amrit Shankar Verma et al. “A probabilistic rainfall model to estimate the leading-edge lifetime of wind turbine blade coating system”. In: *Renewable Energy* 178 (Nov. 2021), pp. 1435–1455. ISSN: 18790682. DOI: 10.1016/j.renene.2021.06.122.

[35] Amrit Shankar Verma et al. “Numerical investigation of rain droplet impact on offshore wind turbine blades under different rainfall conditions: A parametric study”. In: *Composite Structures* 241 (June 2020). ISSN: 02638223. DOI: 10.1016/j.compstruct.2020.112096.

[36] Wangxia Wu et al. “Curved surface effect on high-speed droplet impingement”. In: *Journal of Fluid Mechanics* 909 (2020). ISSN: 14697645. DOI: 10.1017/jfm.2020.926.

[37] Wei Yin et al. “Gas–Solid Erosive Wear of Biomimetic Pattern Surface Inspired from Plant”. In: *Tribology Transactions* 60.1 (Jan. 2017), pp. 159–165. ISSN: 1547397X. DOI: 10.1080/10402004.2016.1154234.

[38] Jun Qiu Zhang et al. “Scorpion back inspiring sand-resistant surfaces”. In: *Journal of Central South University* 20.4 (Apr. 2013), pp. 877–888. ISSN: 20952899. DOI: 10.1007/s11771-013-1561-4.

[39] Junqiu Zhang et al. “The Ingenious Structure of Scorpion Armor Inspires Sand-Resistant Surfaces”. In: *Tribology Letters* 65.3 (Sept. 2017). ISSN: 15732711. DOI: 10.1007/s11249-017-0895-8.

[40] Ruizi Zhang et al. “Effects of droplet shape on impact force of low-speed droplets colliding with solid surface”. In: *Experiments in Fluids* 60.4 (Apr. 2019). ISSN: 07234864. DOI: 10.1007/s00348-019-2712-7.

[41] Han Zhiwu et al. “Erosion resistance of bionic functional surfaces inspired from desert scorpions”. In: *Langmuir* 28.5 (Feb. 2012), pp. 2914–2921. ISSN: 07437463. DOI: 10.1021/la203942r.

[42] Wen Ping Zhou and Mao Li Yang. “Dynamic response of wind turbine blade surface material under water droplet high velocity impact”. In: *Journal of Physics: Conference Series*. Vol. 2306. 1. Institute of Physics, 2022. DOI: 10.1088/1742-6596/2306/1/012016.

A

LS-DYNA keywords

A.1. Sections

*SECTION_SOLID_(TITLE) (1)

(Can not edit keyword since it is associated with post D3PLOT)

TITLE							
sample_sec							
SECID	ELFORM	AET	UNUSED	UNUSED	UNUSED	COHOFF	GASKEIT
1	16	0				0.0	0.0

Figure A.1: Section of the sample

*SECTION_SPH_(TITLE) (1)

(Can not edit keyword since it is associated with post D3PLOT)

TITLE							
droplet_sec							
SECID	CSLH	HMIN	HMAX	SPHINI	DEATH	START	SPHKERN
2	1.2000000	0.2000000	2.0000000	0.0	1.000e+20	0.0	0

Figure A.2: Section of the droplet

A.2. Materials and EOS

*MAT_PIECEWISE_LINEAR_PLASTICITY_(TITLE) (024) (1)

TITLE							
Epoxy							
MID	RO	E	PR	SIGY	ETAN	FAIL	TDEL
1	0.0028200	7.000e+04	0.3000000	240.00000	2.700e+04	1.000e+21	0.0
C	P	LCSS	LCSR	VP			
0.0	0.0	0	0	0.0			
EPS1	EPS2	EPS3	EPS4	EPS5	EPS6	EPS7	EPS8
0.0	0.0	0.0	0.0	0.0	0.0	0.0	0.0
ES1	ES2	ES3	ES4	ES5	ES6	ES7	ES8
0.0	0.0	0.0	0.0	0.0	0.0	0.0	0.0

Figure A.3: Material model for the epoxy sample

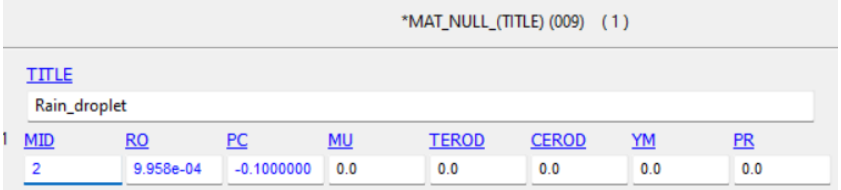

Figure A.4: Material model for the droplet

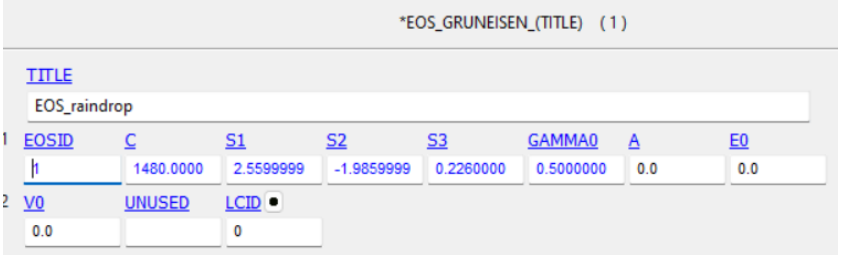

Figure A.5: Equations of state of the droplet

A.3. Boundary conditions

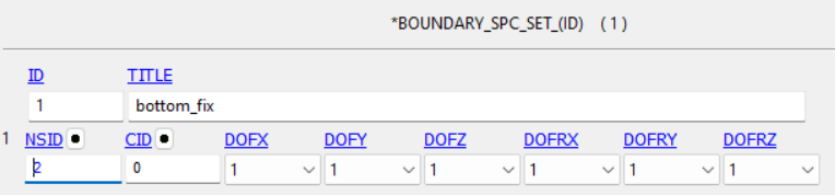

Figure A.6: Fixation of bottom face of sample

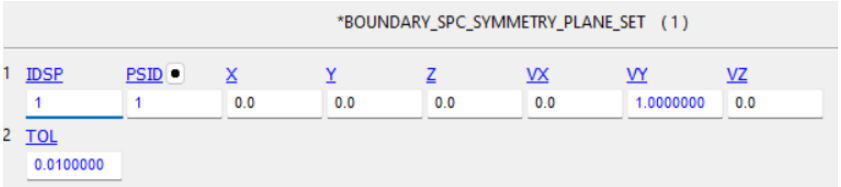

Figure A.7: Symmetry condition of the sample

Figure A.8: Symmetry condition of the droplet

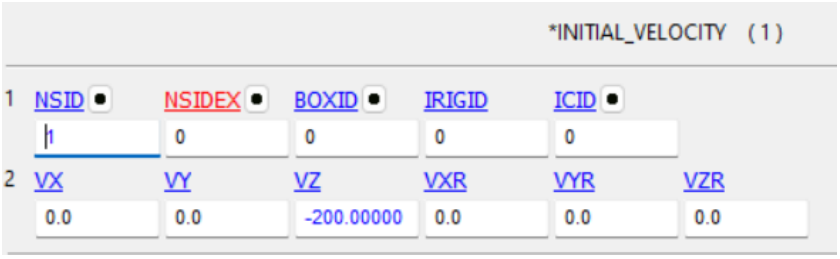

Figure A.9: Initial velocity of droplet

A.4. Contact

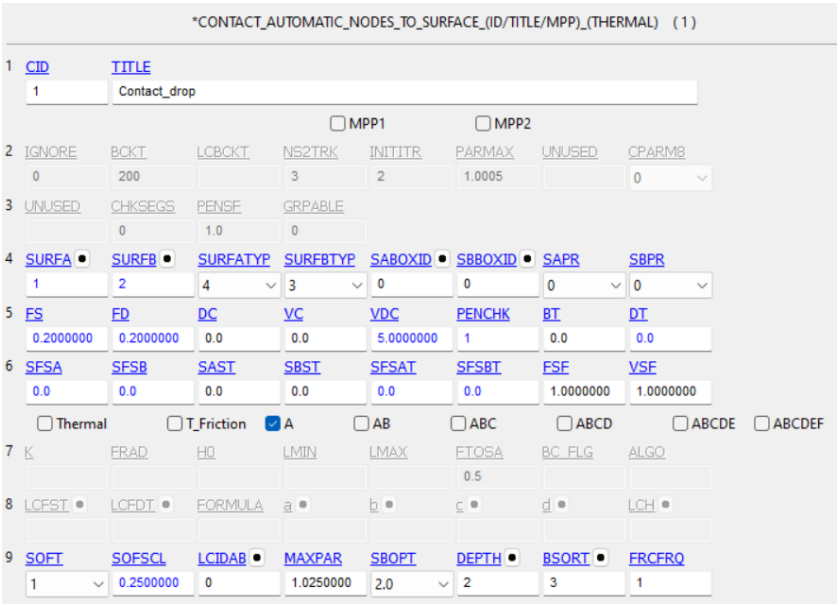

Figure A.10: Contact keyword between droplet and sample

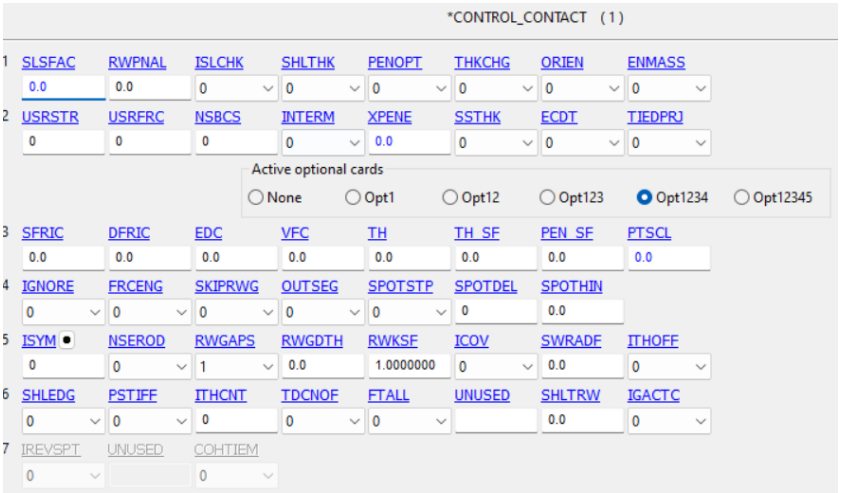

Figure A.11: Control keyword for the contact

A.5. Control

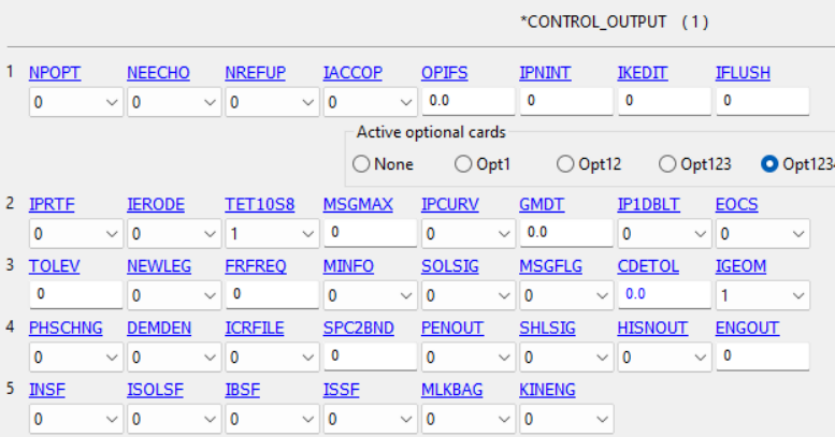

Figure A.12: Control keyword for the output parameters

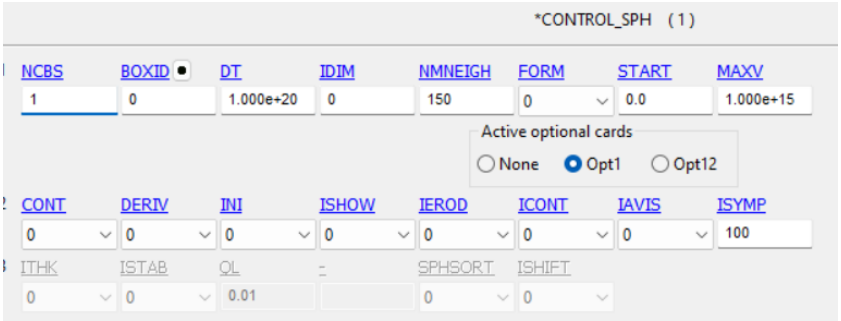

Figure A.13: Control keyword for the SPH model